

## RAS-NAAD: 40-yr High-Resolution North Atlantic Atmospheric Hindcast for Multipurpose Applications (New Dataset for the Regional Mesoscale Studies in the Atmosphere and the Ocean)

ALEXANDER GAVRIKOV,<sup>a</sup> SERGEY K. GULEV,<sup>a,b</sup> MARGARITA MARKINA,<sup>a,b</sup> NATALIA TILININA,<sup>a</sup>  
POLINA VEREZEMSKAYA,<sup>a</sup> BERNARD BARNIER,<sup>a,c</sup> AMBROISE DUFOUR,<sup>a,c</sup> OLGA ZOLINA,<sup>a,c</sup>  
YULIA ZYULYAEVA,<sup>a</sup> MIKHAIL KRINITSKIY,<sup>a</sup> IVAN OKHLOPKOV,<sup>b</sup> AND ALEXEY SOKOV<sup>a</sup>

<sup>a</sup> *P.P. Shirshov Institute of Oceanology, Russian Academy of Sciences, Moscow, Russia*

<sup>b</sup> *Moscow State University, Moscow, Russia*

<sup>c</sup> *Institut des Géosciences de l'Environnement, Grenoble, France*

(Manuscript received 2 August 2019, in final form 3 March 2020)

### ABSTRACT

We present in this paper the results of the Russian Academy of Sciences North Atlantic Atmospheric Downscaling (RAS-NAAD) project, which provides a 40-yr 3D hindcast of the North Atlantic (10°–80°N) atmosphere at 14-km spatial resolution with 50 levels in the vertical direction (up to 50 hPa), performed with a regional setting of the WRF-ARW 3.8.1 model for the period 1979–2018 and forced by ERA-Interim as a lateral boundary condition. The dataset provides a variety of surface and free-atmosphere parameters at sigma model levels and meets many demands of meteorologists, climate scientists, and oceanographers working in both research and operational domains. Three-dimensional model output at 3-hourly time resolution is freely available to the users. Our evaluation demonstrates a realistic representation of most characteristics in both datasets and also identifies biases mostly in the ice-covered regions. High-resolution and nonhydrostatic model settings in NAAD resolve mesoscale dynamics first of all in the subpolar latitudes. NAAD also provides a new view of the North Atlantic extratropical cyclone activity with a much larger number of cyclones as compared with most reanalyses. It also effectively captures highly localized mechanisms of atmospheric moisture transports. Applications of NAAD to ocean circulation and wave modeling are demonstrated.

### 1. Introduction

Subsynoptic and mesoscale atmospheric dynamics over the North Atlantic Ocean are of great interest for understanding the mechanisms of highly localized precipitation, heat and moisture transports, and low-level baroclinicity in the atmosphere. Changes in the intensity and location of the North Atlantic storm tracks are critically important for the quantification of the impact of highly variable atmospheric processes onto air–sea fluxes and associated ocean signals and for understanding the responses of cyclone activity to those ocean signals (Minobe et al. 2008, 2010; Woollings et al. 2012; Tilinina et al. 2018). Many works hint at the critical role

of mesoscale dynamics in air–sea interaction in the North Atlantic, first of all in forming cold-air outbreaks (Zolina and Gulev 2003; Bond and Cronin 2008; Papritz et al. 2015; Kim et al. 2016) over the Gulf Stream, the Labrador Sea, and the Greenland–Iceland–Norwegian (GIN) Seas and in generating polar lows characterized by small scales and extreme surface fluxes in the subpolar regions (Kolstad 2011; Condron and Renfrew 2013; Stoll et al. 2018, among others). Extremely high turbulent heat and momentum surface fluxes associated with these phenomena are highly localized in space and in time and require high temporal and spatial resolution for their adequate representation in models (Gulev and Belyaev 2012; Vihma et al. 2014).

Many lower-troposphere responses to the ocean signals are also associated with mesoscale processes, including the low-level baroclinicity over the western boundary currents (Nakamura et al. 2012; Ogawa et al. 2012; Small et al. 2014; Ma et al. 2017; DuVivier et al. 2016;

 Denotes content that is immediately available upon publication as open access.

Corresponding author: Sergey K. Gulev, gul@sail.msk.ru

DOI: 10.1175/JAMC-D-19-0190.1

© 2020 American Meteorological Society. For information regarding reuse of this content and general copyright information, consult the [AMS Copyright Policy](https://www.ametsoc.org/PUBSReuseLicenses) ([www.ametsoc.org/PUBSReuseLicenses](https://www.ametsoc.org/PUBSReuseLicenses)).

Parfitt et al. 2016, 2017) and anomalous convective precipitation in warm seasons (Minobe et al. 2008; Hand et al. 2014). High-resolution regional model experiments demonstrated the responses of the lower atmosphere to the ocean signals at length scales of less than 30–50 km, suggesting ocean–atmosphere coupling at mesoscales and submesoscales (Small et al. 2008, 2014, 2019; Ma et al. 2017; Parfitt et al. 2016; Bishop et al. 2017). Subsynoptic and mesoscale processes are also crucial for better understanding the mechanisms of atmospheric moisture transports, first of all in the atmospheric rivers (ARs; Lavers et al. 2011; Lavers and Villarini 2015; Gimeno et al. 2014) providing strong ocean-to-continent moisture intrusions associated with abundant precipitation. All of these phenomena cannot always be adequately captured by global reanalyses, such as ERA-Interim, JRA-55, MERRA-2, and ERA5 (Dee et al. 2011; Kobayashi et al. 2015; Gelaro et al. 2017; Copernicus Climate Change Service 2017; for definitions of acronyms, see <https://www.ametsoc.org/PubsAcronymList>), partly because of their relatively coarse resolution but also because of the use of hydrostatic model configurations. Remarkably, the Arctic System Reanalysis (ASR; Bromwich et al. 2016, 2018) performed with the polar Weather Research and Forecasting (WRF) Model (Bromwich et al. 2009) demonstrated a considerable improvement of the representation of many phenomena in the Arctic atmosphere (Tilinina et al. 2014; Moore et al. 2015, 2016; Smirnova and Golubkin 2017; Boisvert et al. 2018; Justino et al. 2019, among others).

Ongoing ocean modeling activities also require high-resolution forcing functions accounting for mesoscale atmospheric features. Existing datasets used for forcing model experiments such as Drakkar forcing set (DFS4/5), Coordinated Ocean-Ice Reference Experiments (CORE), and JRA-55-do are based on global reanalyses (Large and Yeager 2004, 2009; Brodeau et al. 2010; Danabasoglu et al. 2014, 2016; Tsujino et al. 2018) with a spatial resolution of approximately 50–100 km. At the same time, modern eddy-resolving ocean general circulation models use resolutions finer than  $1/10^\circ$ , equivalent to a few kilometers at subpolar latitudes (Deshayes et al. 2013; Sérazin et al. 2015; Guo et al. 2014; Rudnick et al. 2015; Behrens et al. 2017), and up to  $1/50^\circ$ – $1/60^\circ$  in some regional simulations (Chassignet and Xu 2017; Fresnay et al. 2018; Fallmann et al. 2019). These experiments are focused on essentially small-scale ocean features. The role of small-scale atmospheric processes, however, remains unclear when using relatively coarse-resolution forcing. Similarly, modern spectral wave models account for highly nonlinear wave generation and development processes strongly dependent on the submesoscale wind

structure (Ardhuin et al. 2012; Hanley et al. 2010; Semedo et al. 2011; Zieger et al. 2015; Markina et al. 2019). At the same time, in most cases these advanced configurations are forced with relatively coarse-resolution reanalysis winds.

In summary, there is a high demand from different communities for long-term high-resolution atmospheric hindcasts performed with high-resolution model configurations for the North Atlantic where mesoscale and submesoscale processes are of high relevance. Facing this challenge, the P.P. Shirshov Institute of Oceanology of the Russian Academy of Sciences (IORAS) in cooperation with the Institut des Géosciences de l'Environnement (IGE) developed a high-resolution (14 km) atmospheric downscaling experiment for the North Atlantic Ocean [North Atlantic Atmospheric Downscaling (NAAD)]. In NAAD, the nonhydrostatic WRF Model was forced at the lateral boundaries by the ERA-Interim reanalysis over the 40-yr period (1979–2018). In the following, we describe the NAAD model configuration and production strategy in section 2 followed by a short description of NAAD products and data availability (section 3). Then we turn to the NAAD evaluation (section 4) and pilot applications (section 5). In the conclusive section 6 we discuss the NAAD added value and perspectives of further developments of the product.

## 2. NAAD model configuration and production strategy

In NAAD we used the nonhydrostatic WRF Model, version 3.8.1 (Skamarock et al. 2008; Powers et al. 2017). The domain covers the North Atlantic from  $10^\circ$  to  $80^\circ\text{N}$  and from  $90^\circ\text{W}$  to  $5^\circ\text{E}$  (Fig. 1), with the center at  $45^\circ\text{N}$ ,  $45^\circ\text{W}$ . The initial and lateral boundary conditions [including sea surface temperature (SST)] were provided by the ERA-Interim reanalysis (Dee et al. 2011) at  $0.7^\circ \times 0.7^\circ$  spatial resolution and 60 levels in the vertical direction. The spatial resolution in the basic NAAD high-resolution experiment (HiRes) was 14 km ( $551 \times 551$  points) and 50 terrain-following, dry hydrostatic pressure levels, starting from around 10–12 m above the ocean surface to 50 hPa with  $\sim 15$  levels in the boundary layer (<http://www.naad.ocean.ru>). Besides the HiRes experiment, we also conducted a moderately low resolution experiment (LoRes) with the hydrostatic setting of the WRF Model at 77-km resolution ( $110 \times 110$  points) with 50 vertical levels (as in HiRes). The LoRes experiment (with resolution comparable to ERA-Interim) will be used to quantify the added value of the HiRes experiment, which cannot be directly compared with ERA-Interim (constrained by

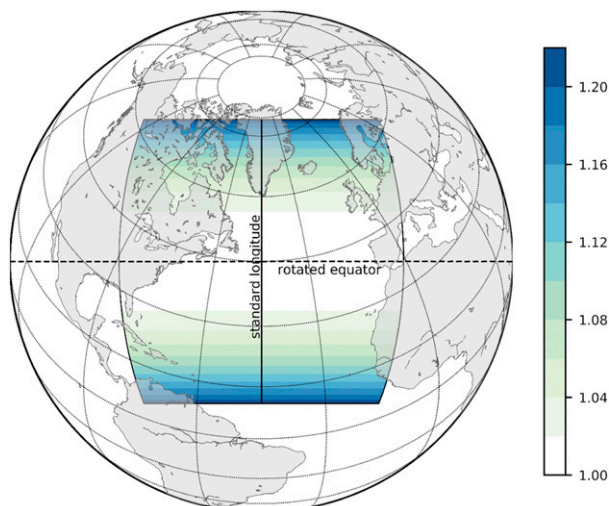


FIG. 1. NAAD computational domain and map-scale factor for the HiRes simulation.

data assimilation and using a very different model configuration). All experiments were run for the 40-yr period from January 1979 to December 2018. Details of the model settings for the HiRes and LoRes experiments are presented in Table 1.

Most parameterizations were used in both HiRes and LoRes NAAD experiments. We used the Kain–Fritsch (KF) convective parameterization scheme (Kain 2004). The RRTMG longwave and shortwave

radiation schemes (Iacono et al. 2008) were used for terrestrial and solar radiation processes, which additionally utilize effective cloud water, ice and snow radii from the single-moment 6-class (WSM6) scheme for microphysics (Hong and Lim 2006) in HiRes, and subgrid convective cloud information from KF for a more accurate estimation of atmospheric optical depth. The surface layer was parameterized by the MM5 scheme of (Skamarock et al. 2008) based upon similarity theory, accounting for a viscous sublayer and incorporating the COARE 3.0 algorithm (Fairall et al. 2003) for calculating thermal and moisture roughness lengths (or exchange coefficients for heat and moisture) over the ocean surface. For the planetary boundary layer (PBL) we used the Yonsei University (YSU) nonlocal scheme (Hong et al. 2006) and the Noah land surface model (Chen and Dudhia 2001). An important issue is the number of vertical levels captured by the PBL. In NAAD (see the specification of vertical levels at <http://www.naad.ocean.ru>), 15 vertical levels are below 850 hPa. Computation of the PBL height (not shown) reveals the highest PBL exceeding 1000 m over the regions with active convection and the lowest PBL of less than 200 m in the polar regions. This implies that the number of vertical levels in PBL range from as few as 5–6 to as many as 15–16 over the NAAD domain. In this respect, for example, version 2 of ASR (ASRv2; Bromwich et al. 2018) with approximately 10–12 levels in the PBL (implied by 25 levels below

TABLE 1. NAAD HiRes and LoRes experimental design (see text for details).

Attribute	Setting	
	General	
Model	WRF-ARW 3.8.1	
Name of expt	LoRes	HiRes
Dynamical core	Hydrostatic	Nonhydrostatic
	Grid and time configuration	
Horizontal grid type	Arakawa C grid staggered	
Horizontal resolution	77 km	14 km
Vertical coordinate type	Terrain-following, dry hydrostatic pressure	
Vertical resolution, no. of levels	50	
Time-stepping scheme	Time-split integration using a third-order Runge–Kutta scheme	
Time step (s)	240	30
	Physical parameterizations	
Microphysics scheme	WSM5 (Hong et al. 2004)	WSM6 (Hong and Lim 2006)
Cumulus scheme	Kain–Fritsch (Kain 2004)	
PBL scheme	YSU (Hong et al. 2006)	
Surface-layer scheme	MM5 (Skamarock et al. 2008)	
Radiative transfer (short- and longwave)	RRTMG (Iacono et al. 2008)	
Land surface model	Noah LSM (Chen and Dudhia 2001)	
	Boundary conditions	
Initial and boundary conditions	ERA-Interim (spectral nudging longer than 1100 km)	
SST	ERA-Interim	

850 hPa) is more effective in polar latitudes; however, ASRv2 is based on the local Mellor–Yamada–Janjić PBL scheme, which may not necessarily be effective over the whole North Atlantic region.

Since the Noah scheme updates deep soil temperature, the skin sea surface temperature is calculated using the Zeng and Beljaars (2005) formulation. The PBL scheme is responsible for vertical subgrid-scale fluxes due to eddy transports in the whole atmospheric column, and not only in the boundary layer. Horizontal eddy viscosity coefficients are obtained in the WRF dynamic core independently using the Smagorinsky first-order closure approach. Parameterizations of microphysics were nevertheless different in HiRes and LoRes. Thus, the WSM6 scheme for microphysics (Hong and Lim 2006) was used in the NAAD-HiRes and WSM 5-class (WSM5; Hong et al. 2004). Additionally, employing entrainment information from KF was applied in the NAAD-LoRes case. For the long-term runs with WRF in both HiRes and LoRes experiments, the RRTMG scheme uses climatological ozone and aerosol data. The ozone data were adapted from the Community Atmospheric Model radiation scheme with latitudinal ( $2.82^\circ$  step), height, and temporal (monthly) variation. The aerosol data were based on the Tegen et al. (1997) dataset with relatively coarse spatial ( $5^\circ$  in longitude and  $4^\circ$  in latitude) and temporal (monthly) resolution.

The WRF settings used for NAAD HiRes, with some modifications, was applied in a number of applications. In the Polar WRF used in ASRv2 (Bromwich et al. 2018) the major difference was in the use of the Mellor–Yamada–Nakanishi–Niino (Nakanishi 2001; Nakanishi and Niino 2004, 2006) 2.5-level PBL parameterization. However, the nonlocal YSU scheme used in NAAD is effective to resolve strong convective processes in the midlatitudes and tropical regions. This parameterization was used in a number of RCM simulations (Bukovsky and Karoly 2009; Otte et al. 2012; Gao et al. 2015; Tang et al. 2017).

At the ocean surface, we used ERA-Interim SST and sea ice, which was updated every 6 h during the simulation. ERA-Interim SST is combined from different sources (Dee et al. 2011). Kumar et al. (2013) demonstrated that in different reanalyses, the intraseasonal SST–precipitation relationship is dependent on the SST used. In this respect we understand that the relatively coarse (with respect to HiRes) resolution of ERA-Interim SST may have an effect on the atmospheric surface layer and PBL. Currently, several high-resolution SST datasets, while limited in time coverage, are available (Chelton and Wentz 2005; Chao et al. 2009; Ricchi et al. 2016). Nevertheless, for the 40-yr-long NAAD experiments we used ERA-Interim SST, which is considered to be homogeneous and adequate for multidecadal scales.

To reduce unrealistic atmospheric dynamics in the regional domain in both LoRes and HiRes experiments, we applied throughout the 40-yr period the procedure of spectral interior nudging (Jeuken et al. 1996; Miguez-Macho et al. 2004). The spectral nudging technique optimizes the adjustment of the large-scale dynamics inside the domain to that implied by the boundary conditions. The nudging procedure was applied to the zonal and meridional wind components, air temperature, and the perturbation of the geopotential height. We did not nudge the moisture fields because their variability is not always represented adequately in the coarse-resolution ERA-Interim (Miguez-Macho et al. 2004; Otte et al. 2012). Configuration of nudging was set according to the sensitivity study of Markina et al. (2018), which implied the optimal wavelength cutoff being 1100 km, applied only above the PBL. For determining the optimal nudging strength, we performed sensitivity experiments with the nudging strength coefficients increasing from  $3 \times 10^{-5}$  to  $3 \times 10^{-3} \text{ s}^{-1}$ . These experiments implied an optimal value of the nudging strength coefficient of  $3 \times 10^{-4} \text{ s}^{-1}$  (equivalent to a damping scale of about 1 h). This value is also consistent with other studies (Miguez-Macho et al. 2004; Otte et al. 2012; Tang et al. 2017, among others). Note also that the ASRv2 (Bromwich et al. 2018) used spectral nudging with the strength  $3 \times 10^{-3} \text{ s}^{-1}$  (i.e., an order of magnitude stronger relative to NAAD) for all levels in the outer domain and above 100 hPa in the inner domain. However, a direct comparison is unlikely to be possible here, as the ARSv2 assimilates a lot of observational data in the surface layer using the same technique (Newtonian relaxation, also called “observational nudging”; Jeuken et al. 1996).

The dynamical solver of WRF uses a Cartesian grid. The difference between the geographical and the model horizontal distance (map-scale factor) should not deviate significantly from unity in order to match the CFL criterion. The NAAD grid is based on a cylindrical equidistant projection (*lat-lon* in the namelist; <http://www.naad.ocean.ru>) with the rotated pole in order to locate the equator at the middle of the domain (*pole\_lat* = 45; *pole\_lon* = 180; *stand\_lon* = -45). For this projection, the maximum map-scale factor amounts to 1.2 in the northernmost and southernmost regions of the domain (Fig. 1). This allowed for keeping a constant third-order Runge–Kutta time step of 30 s in HiRes and 240 s in LoRes. In NAAD we used the USGS topography data with 10 min spatial resolution.

### 3. NAAD products and data availability

NAAD products (see <http://www.naad.ocean.ru> for the parameter identification and namelist) include

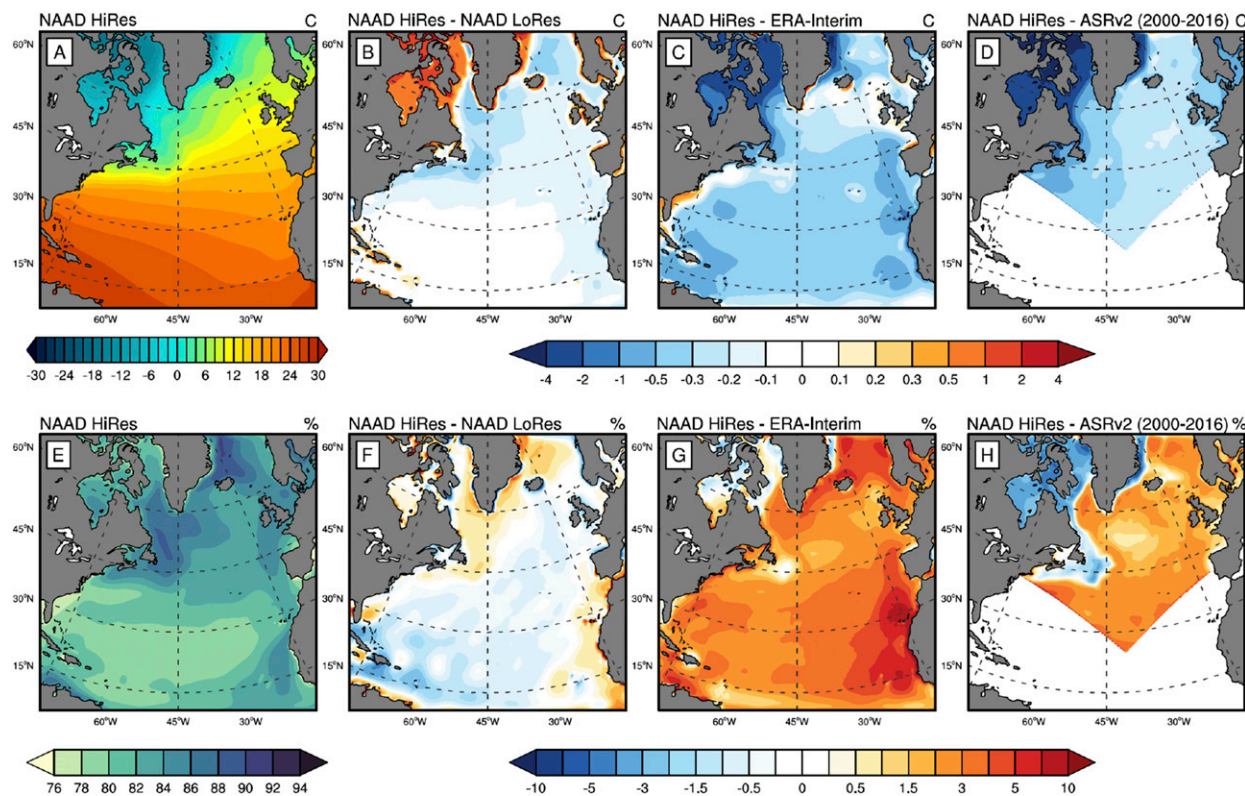


FIG. 2. (a) Annual mean (1979–2018) 2-m air temperature in NAAD HiRes and differences in the annual mean 2-m air temperatures (b) between NAAD HiRes and NAAD LoRes, (c) between NAAD HiRes and ERA-Interim, and (d) between NAAD HiRes and ASRv2. Also shown is (e) annual mean (1979–2018) 2-m relative humidity in NAAD HiRes and differences in the annual mean 2-m relative humidity (f) between NAAD HiRes and NAAD LoRes, (g) between NAAD HiRes and ERA-Interim, and (h) between NAAD HiRes and ASRv2. For LoRes and ERA-Interim, the differences are for the period of 1979–2018; for ASRv2, the differences are for the period of 2000–16.

surface and upper-troposphere variables provided at the native NAAD grid for HiRes and LoRes products with resolutions of 14 and 77 km, respectively, for the period of 1979–2018. Since the NAAD core model (WRF-ARW) uses a staggered Arakawa C grid, all 3D fields are preinterpolated from the C grid on the mass points (unstaggered grid). No interpolation was applied for surface variables and fluxes, provided at the mass points. The entire archive of the NAAD data amounts to 150 terabytes (TB) with individual annual files ranging from approximately 140 MB in LoRes to 3.3 GB in HiRes for surface variables on to 165 GB for HiRes 3D fields. The whole NAAD data output is organized as annual NetCDF files by variable and is available online (<http://www.naad.ocean.ru>) for download using FTP and Network Data Access Protocol (OPeNDAP) accesses.

#### 4. NAAD evaluation

##### a. Surface

Surface-state variables and fluxes are particularly significant as they are used for forcing ocean models and

for the diagnostics of extreme events. Figures 2a and 2b show that surface air temperature diagnosed by NAAD HiRes is colder than in LoRes. The differences between LoRes and HiRes are smaller than  $0.2^{\circ}\text{C}$  over most of the domain and increase to  $0.4^{\circ}\text{C}$  in the western mid-latitude North Atlantic. Larger surface air temperatures in HiRes compared to LoRes, amounting to  $1^{\circ}\text{C}$ , are observed over the ice-covered regions and occur primarily in the winter months. This regional bias can be explained by using a coarse-resolution sea ice mask from ERA-Interim in both HiRes and LoRes NAAD simulations. Compared to ERA-Interim (Fig. 2c), HiRes shows  $0.2^{\circ}$  to  $0.4^{\circ}\text{C}$  lower surface air temperatures over most of the North Atlantic and considerably colder surface air temperatures in the ice-covered regions in the subpolar North Atlantic. A similar pattern of differences in surface air temperature is revealed for ASRv2 (Fig. 2d) for the area of overlap of the two domains. Surface relative humidity (Figs. 2e,f) over open ocean midlatitudes and subtropics is slightly smaller in HiRes compared to LoRes with the differences exceeding 1% identified in the western tropics. At the

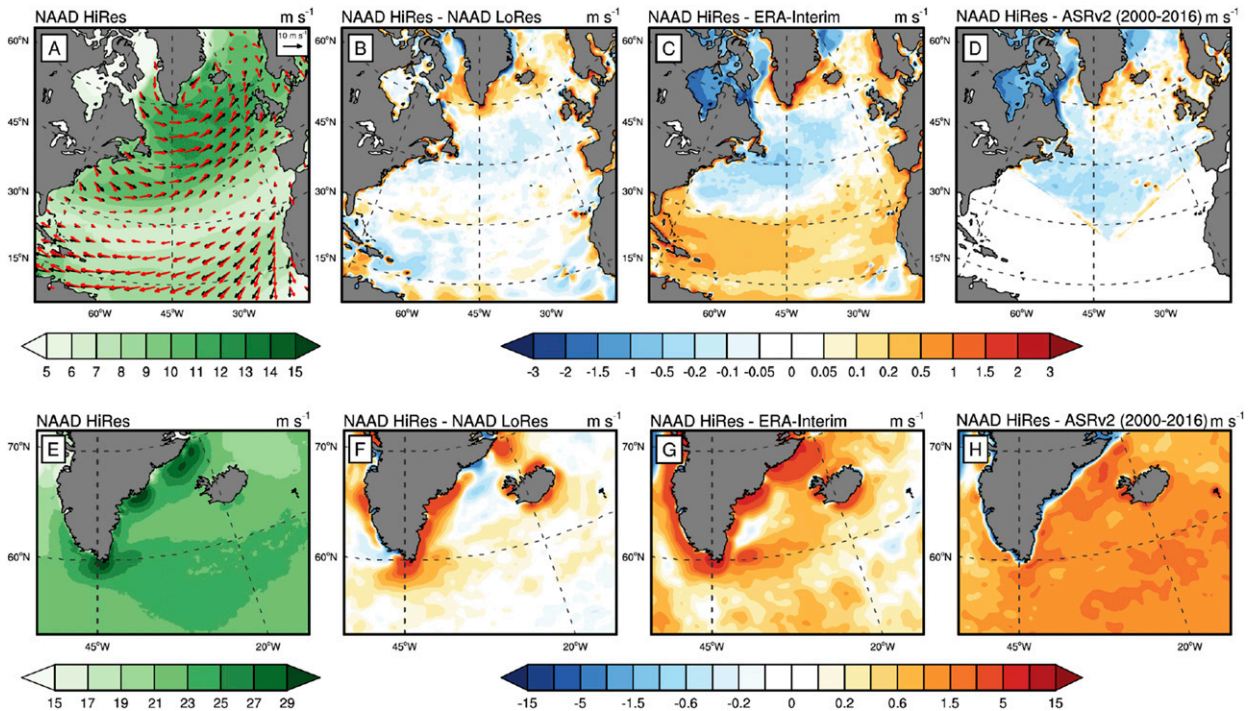


FIG. 3. (a) January mean (1979–2018) scalar 10-m wind speed (colors) in NAAD HiRes and wind vectors in NAAD HiRes (red) and ERA-Interim (black), along with differences in 10-m wind speed (b) between NAAD HiRes and LoRes, (c) between NAAD HiRes and ERA-Interim, and (d) between NAAD HiRes and ASRv2. Also shown is (e) the January 99th percentile of 10-m wind speed over subpolar North Atlantic in NAAD HiRes and differences in 99th percentile of 10-m wind speed (f) between NAAD HiRes and LoRes, (g) between NAAD HiRes and ERA-Interim, and (h) between NAAD HiRes and ASRv2. For LoRes and ERA-Interim, the differences are shown for the period of 1979–2018; for ASRv2, differences are shown for the period of 2000–16.

same time, somewhat more humid surface conditions in HiRes compared to LoRes are identified in the subpolar western North Atlantic and in the offshore region of the subtropical eastern Atlantic. Here the differences amount to 0.6%–0.8%. Compared to ERA-Interim and ASRv2 (Figs. 2g,h), NAAD HiRes shows a relative humidity higher by 2%–3% over the North Atlantic with the strongest differences (>6%) in the eastern North Atlantic subtropics.

Figure 3 shows the evaluation of climatological winter winds in NAAD HiRes and LoRes. NAAD HiRes and LoRes surface winds are consistent south of 45°N with the differences within  $\pm 0.15 \text{ m s}^{-1}$ . At the same time, in the Irminger Sea NAAD HiRes shows stronger mean winds by  $0.2\text{--}0.6 \text{ m s}^{-1}$ , thus likely reflecting a better representation of the mesoscale features such as tip jets and katabatic winds in this area. The comparison with ERA-Interim (Fig. 3c) shows stronger trade winds in the NAAD HiRes experiment, somewhat lower wind speeds in the western midlatitude North Atlantic, and also stronger winds in the subpolar North Atlantic along the eastern Greenland coast. North of 40°N, differences between HiRes and ASRv2 (Fig. 3d) are consistent with

those for ERA-Interim. Dukhovskoy et al. (2017) noted differences between high-resolution satellite wind products and reanalyses attributing them to the subsynoptic and mesoscale processes. The impact of high-resolution and nonhydrostatic setting onto the wind field is especially evident for extreme winds (Figs. 3e–h). We note much stronger katabatic winds and tip jets along the Greenland coast, with the differences in surface winds between HiRes and LoRes experiments being locally over  $4 \text{ m s}^{-1}$  (about 20% of mean values of 99th percentile of wind speed). Relative to ERA-Interim, the HiRes experiment shows extreme winds stronger by more than  $7 \text{ m s}^{-1}$ . Important is that HiRes also shows much better localization of katabatic winds near the coast in HiRes compared to LoRes and ERA-Interim. Figure 3d shows the localization of maximum extreme winds much closer to the Greenland coast in agreement with the case studies (Moore and Renfrew 2005; Moore et al. 2015). Extreme wind speed differences between NAAD HiRes and ASRv2 in the Irminger Sea (Fig. 3h) amount to  $1.5\text{--}2 \text{ m s}^{-1}$ . Comparison of NAAD winds with QuikSCAT winds (Ricciardulli and Wentz 2015) (Fig. 4) indicates that both NAAD HiRes and LoRes have considerably

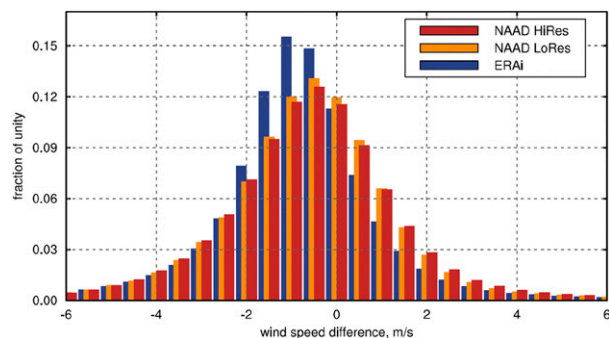


FIG. 4. Histograms of the differences between NAAD HiRes (red), NAAD LoRes (orange), and ERA-Interim (blue) winds with respect to QuikSCAT winds for 2005.

smaller errors with respect to QuikSCAT when compared with ERA-Interim, which clearly demonstrates a systematic negative bias of  $0.5\text{--}2\text{ m s}^{-1}$ .

Surface turbulent fluxes (sensible plus latent, Fig. 5) in NAAD HiRes show the structure to be consistent with reanalyses and blended climatologies such as OA-FLUX (e.g., Yu and Weller 2007) with the locally strong fluxes over the Gulf Stream (primarily due to latent heat) and in the Labrador Sea (mostly due to sensible heat). NAAD HiRes turbulent fluxes are generally larger than those of NAAD LoRes by  $0\text{--}10\text{ W m}^{-2}$  in the open ocean regions and by  $\sim 30\text{ W m}^{-2}$  over the Gulf Stream and in the Labrador and Irminger Seas. In the subpolar latitudes, the stronger HiRes fluxes are explained by the differences in wind speed (Fig. 3) with a significant contribution from surface temperature and humidity gradients, especially for sensible heat flux (no figure shown). In the midlatitudes and subtropics, the differences in turbulent heat fluxes between HiRes and LoRes are associated with surface temperature and humidity vertical gradients, as wind speed differences here are close to zero (Fig. 3). Differences with ERA-Interim (Fig. 5c) are 30%–50% larger than those with NAAD LoRes, while the direct comparison here is difficult because of the differences between the ERA-Interim surface flux algorithm and the COARE 3.0 flux algorithm (Fairall et al. 2003) used in NAAD (Brodeau et al. 2017). Of interest is also the evaluation of extreme surface turbulent fluxes, which might be strongly dependent on mesoscale processes (Ma et al. 2015) and demonstrate differences between different products not consistent with those for mean values (Gulev and Belyaev 2012; Bentamy et al. 2017). Figures 5d–f presents extreme fluxes quantified by the 99th percentile of the modified Fisher–Tippett distribution (Gulev and Belyaev 2012). Relative to LoRes, HiRes shows stronger extreme fluxes over the Gulf Stream

and the North Atlantic Current where differences may locally exceed  $30\text{ W m}^{-2}$  (up to 5%–10% of the mean values). In the Irminger Sea the differences amount to  $200\text{ W m}^{-2}$ , being more than 20%–25% of the mean values of extreme turbulent fluxes. Extreme fluxes diagnosed by HiRes are also considerably stronger than in ERA-Interim (Fig. 5f), with maximum differences locally exceeding  $300\text{ W m}^{-2}$ .

### b. Storm tracks and cyclone dynamics

NAAD opens a new avenue in the analysis of cyclone dynamics and storm tracks. Cyclone tracks were diagnosed using the IORAS algorithm (Zolina and Gulev 2002; Tilinina et al. 2013), tested within the IMILAST project (Neu et al. 2013). Tracking was performed on the NAAD HiRes grid. For tracking cyclones in the limited area over the North Atlantic we applied an approach that accounts for the so-called entry–exit uncertainties (Tilinina et al. 2014). Postprocessing was further applied to cutoff cyclones with migration distances smaller than 1000 km and lifetimes shorter than 24 h (Tilinina et al. 2013).

NAAD HiRes (Fig. 6a) captures well the main North Atlantic storm tracks that are consistent with cyclone climatologies based on the global reanalyses (e.g., Neu et al. 2013; Tilinina et al. 2013). NAAD HiRes shows 30%–60% larger local cyclone numbers compared to LoRes. Also, NAAD LoRes shows slightly larger number of cyclones compared to ERA-Interim while the differences are within 3%–5%. Over the North Atlantic storm track, the number of cyclones in NAAD HiRes is close to that in ERA5 (Fig. 6d) with slightly larger cyclone counts over the storm formation region in the Northwest Atlantic and slightly smaller counts in the central North Atlantic and the subpolar regions.

Figure 7 shows the winter [December–February (DJF)] time series of the domain integrated number of cyclones with different intensities (quantified by central pressure). NAAD HiRes allows for identification of  $\sim 2$  times more cyclones compared to LoRes, which indicates a high consistency with the global reanalyses, except for ERA5, which reveals practically the same number of cyclones as NAAD HiRes (Fig. 7a). Importantly, these differences between HiRes and all other products (including LoRes) are formed mostly by moderately deep and shallow cyclones (Figs. 7b,d). At the same time, the number of deep cyclones in HiRes is more consistent with LoRes and reanalyses showing 10%–15% higher counts. Overall, the winter cyclone activity in NAAD is very close to that in ERA5 and considerably more intense compared to the other reanalyses. Summer results

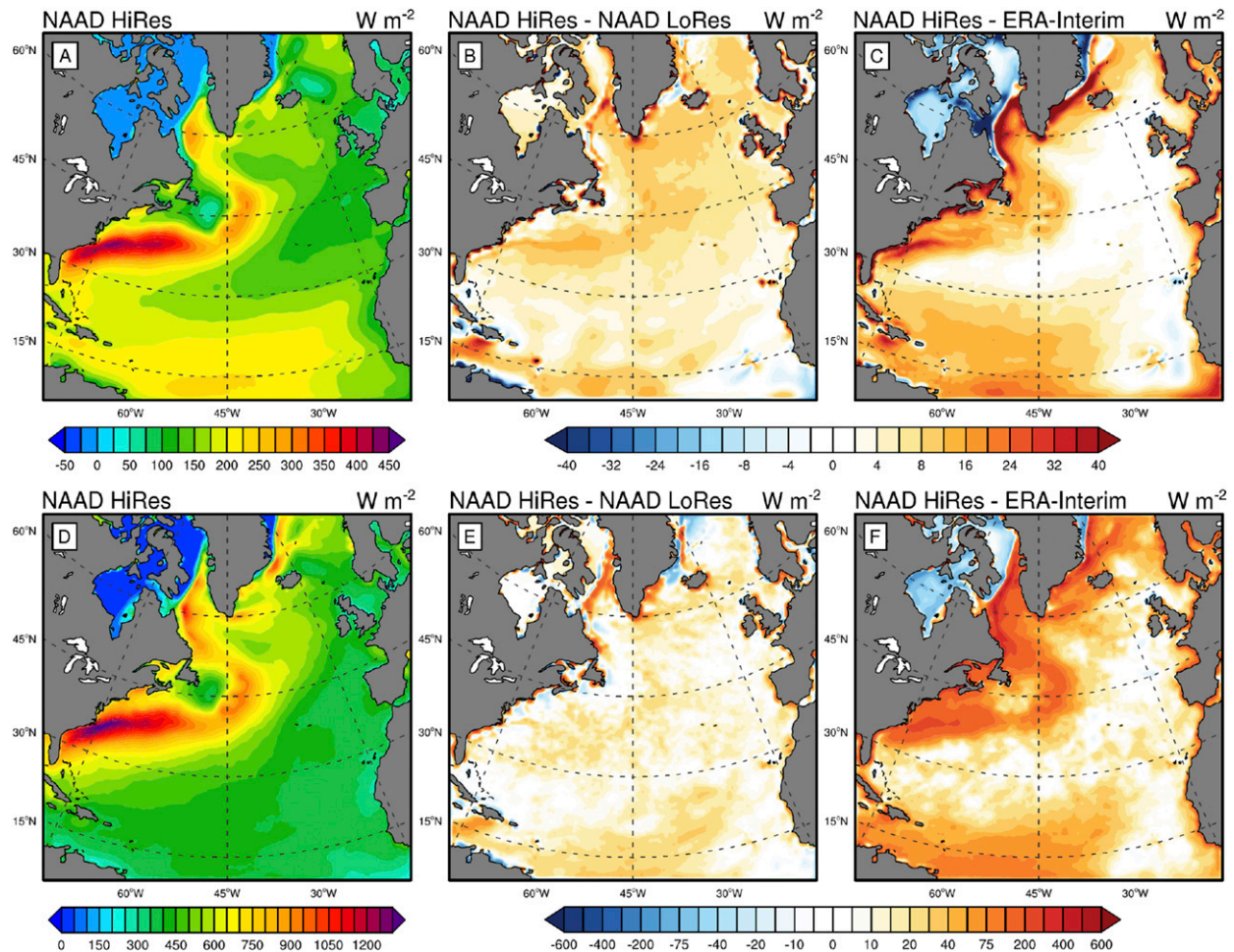


FIG. 5. (a) January (1979–2018) sensible plus latent turbulent heat fluxes in NAAD HiRes and differences in sensible plus latent turbulent heat flux (b) between NAAD HiRes and LoRes and (c) between NAAD HiRes and ERA-Interim. Also shown is the (d) January (1979–2018) 99th percentile of sensible plus latent turbulent heat flux in NAAD HiRes and differences in 99th percentile of sensible plus latent turbulent heat flux (e) between NAAD HiRes and LoRes and (f) between NAAD HiRes and ERA-Interim.

(not shown) are qualitatively similar with even higher differences especially for shallow cyclones dominating during the warm season.

Figure 6 demonstrates relatively strong differences between cyclone counts in NAAD and in all reanalyses over the North American continent. This is likely associated with the fact that the finer-resolution NAAD HiRes is capable of identifying cyclone generation events at an earlier stage than the global reanalyses. Our analysis of cyclogenesis events (not shown) demonstrates considerably larger counts of cyclone generation events over the North American storm track in NAAD when compared with even ERA5, while the total number of tracks is close in both products (Fig. 7). Also, we note that the cyclone effective radius, characterizing cyclone size (Rudeva and Gulev 2007) is smaller in

NAAD HiRes by about 50–100 km as compared with NAAD LoRes and is also smaller by 100–150 km relative to ERA-Interim (no figure shown). NAAD HiRes also demonstrates capabilities in capturing characteristics of extreme cyclones. Thus, our analysis of extremely deep cyclones shows that the 100 deepest cyclones in NAAD HiRes have a central pressure about 4 hPa lower than those in LoRes and ERA-Interim. Similar conclusions were drawn from WRF-based high-resolution ASR in comparison with global reanalyses (Tilinina et al. 2014).

### c. Hydrological cycle

Evaluation of the North Atlantic hydrological cycle in the NAAD is of special interest. Figure 8a shows time series of annual mean precipitation over the NAAD

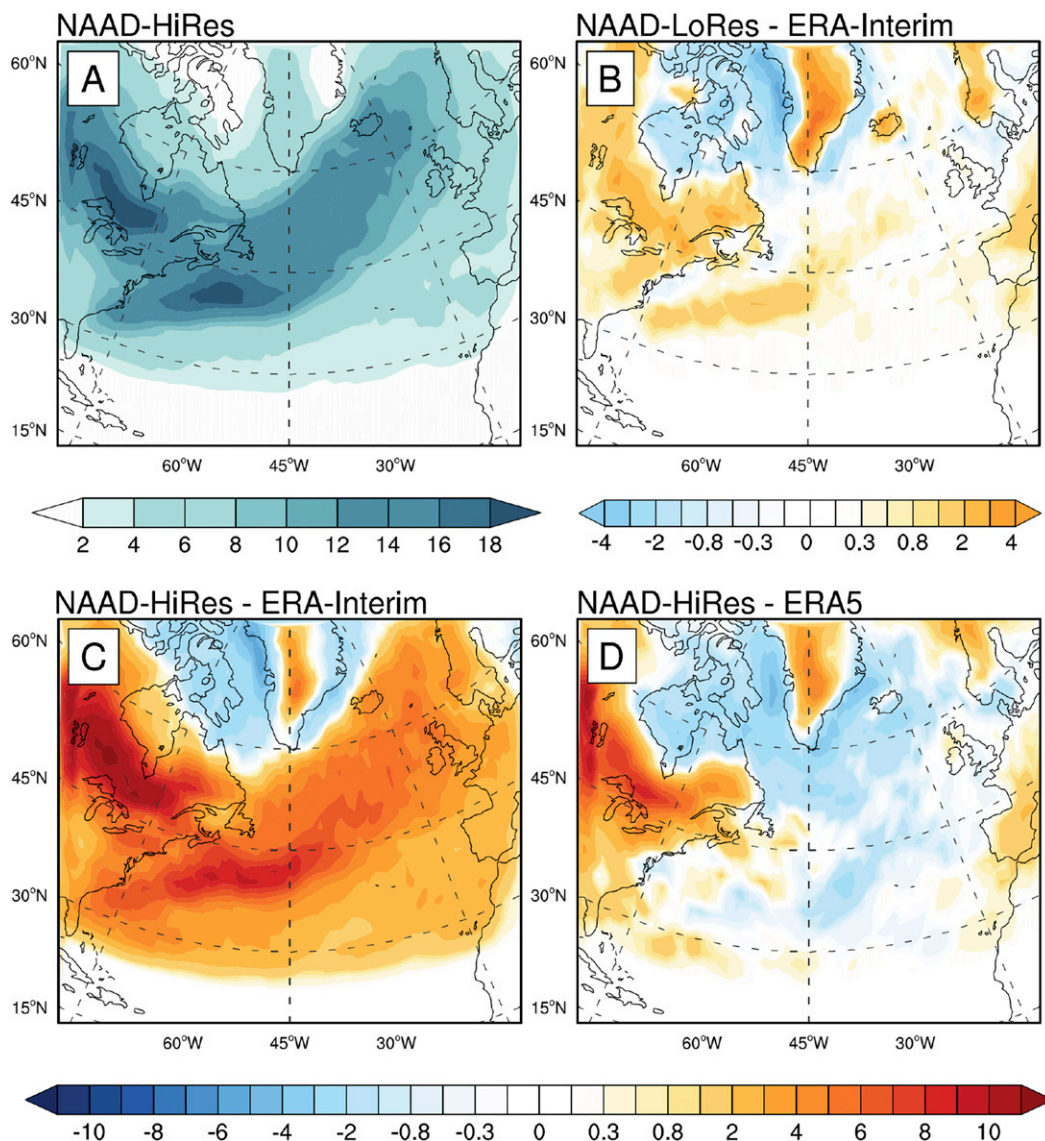


FIG. 6. (a) Winter (DJF; 1979–2018) number of cyclones in NAAD HiRes and the differences in the DJF number of cyclones (b) between NAAD LoRes and ERA-Interim, (c) between NAAD HiRes and ERA-Interim, and (d) between NAAD HiRes and ERA5. Units are cyclone tracks per season (DJF) per circle with a radius of 2° latitude [equivalent to approximately 155 000 km<sup>2</sup>; see [Tilinina et al. \(2013, 2014\)](#) for the mapping metrics].

domain as computed from NAAD HiRes and LoRes experiments, as well as from ERA-Interim, the Global Precipitation Climatology Project (GPCP1DD) ([Huffman et al. 2001](#)), and, starting from 2013, the Global Precipitation Measurement (GPM) mission ([Skofronick-Jackson et al. 2017](#)). NAAD HiRes shows slightly higher domain integrated total precipitation values compared to NAAD LoRes before the early 2000s and slightly smaller precipitation during the last 15 years. Both HiRes and LoRes domain integrated values are 4%–7% less than ERA-Interim and 5%–10% less than GPCP. Starting from

2013, NAAD HiRes is in a very good agreement with GPM, demonstrating very small (relative to the other products) differences for all seasons ([Fig. 8b](#)). The consistency with GPM is, however, somewhat better in autumn–winter than in spring–summer, likely because of a stronger contribution of the convective precipitation (requiring even higher resolution than that in HiRes) during the warm season.

[Figures 9a–c](#) shows annual mean total precipitation in NAAD HiRes and the differences with LoRes and ERA-Interim. NAAD HiRes when compared with

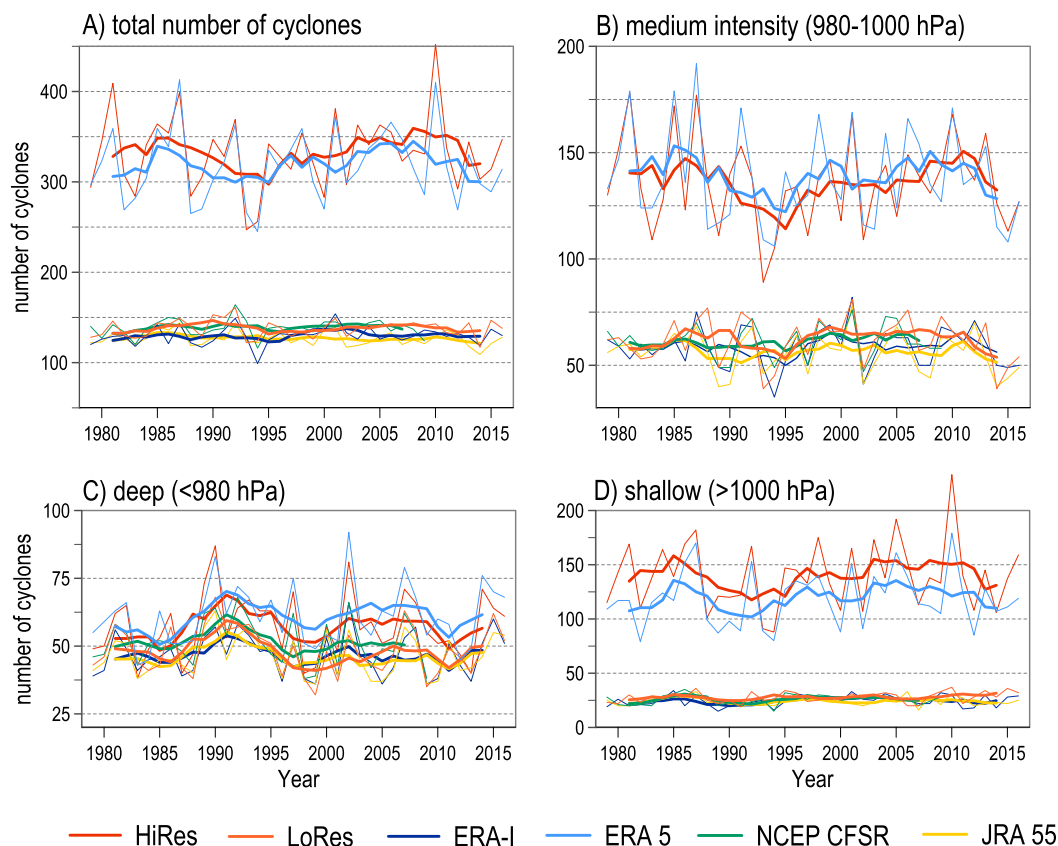


FIG. 7. Time series of the seasonal (DJF) (a) total number of cyclones, as well as numbers of (b) moderately deep, (c) deep, and (d) shallow cyclones in NAAD HiRes, NAAD LoRes, and different reanalyses. Thin lines show winter (DJF) annual values, and thick lines show 5-yr running means.

LoRes shows stronger precipitation in the western Atlantic tropics and over the Gulf Stream by up to  $1 \text{ mm day}^{-1}$  and lower, by  $0.3\text{--}0.5 \text{ mm day}^{-1}$ , precipitation in the North Atlantic subpolar gyre. Relative to ERA-Interim (Fig. 9c), NAAD HiRes shows stronger precipitation over the Gulf Stream (up to  $2 \text{ mm day}^{-1}$ ) and weaker precipitation over the subpolar latitudes. The precipitable water content (PWC) (Figs. 9d,e) is lower in NAAD HiRes than in LoRes by 4%–6%, with the strongest absolute differences in the western tropics. ERA-Interim, however, shows a slightly higher PWC than NAAD HiRes over most of the domain except for the western tropics and subtropics (Fig. 9e). Differences in precipitation and PWC suggest stronger tropical water recycling in NAAD HiRes and somewhat weaker recycling in mid- and subpolar latitudes relative to LoRes and ERA-Interim.

Representation of summer precipitation over the western North Atlantic is important for quantifying the lower-atmosphere responses to the ocean frontal signals in the Gulf Stream (Minobe et al. 2008, 2010; Parfitt et al. 2016). Precipitation responses in summer are

typically associated with convective processes and mostly located over the westernmost part of the Gulf Stream. In winter, precipitation responses are associated with the atmospheric frontal activity and enhanced precipitation over the central and eastern Gulf Stream proper (Minobe et al. 2010). Figure 10 demonstrates precipitation for July 2015 as revealed by NAAD HiRes and LoRes as well as by ERA-Interim, ERA5, GPM, and GPCP. NAAD HiRes with its capability to capture convective processes shows the best agreement with GPCP in the structure of precipitation pattern and in magnitude. NAAD LoRes and ERA-Interim tend to underestimate precipitation rates by  $2\text{--}4$  and  $3\text{--}6 \text{ mm day}^{-1}$ , respectively. ERA5 is most consistent with HiRes in spatial structure but shows smaller precipitation rates of  $2\text{--}3 \text{ mm day}^{-1}$ . Comparison with ASRv2 (no figure shown) is somewhat difficult as the ASR domain boundary cuts a considerable part of the region analyzed. However, for the overlapping part of the domain the precipitation pattern in ASRv2 is comparable in structure to that of NAAD HiRes.

Capabilities of the high-resolution NAAD in representing moisture transports can be analyzed through the

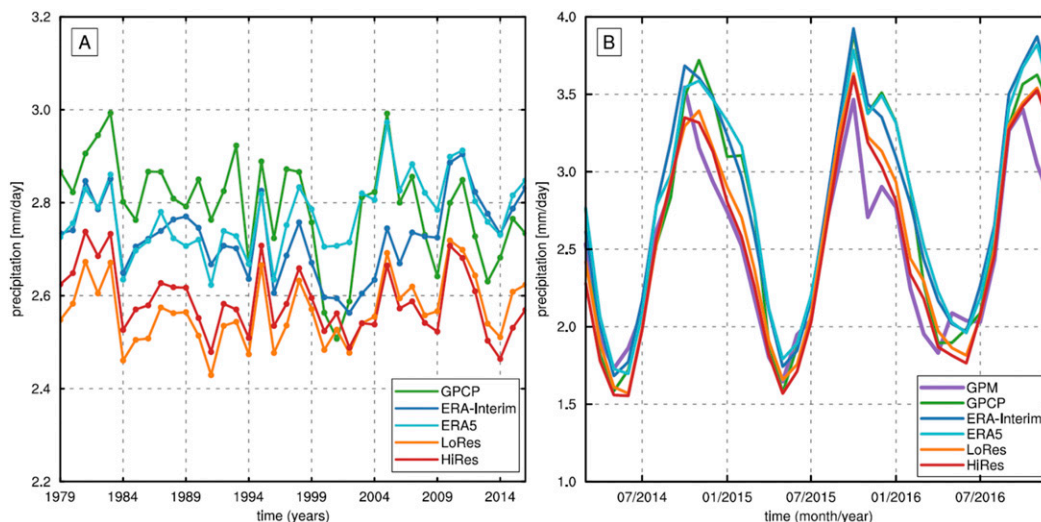


FIG. 8. Time series of the (a) annual mean domain-averaged precipitation ( $\text{mm day}^{-1}$ ) for 1979–2017 and (b) monthly mean domain-averaged precipitation ( $\text{mm day}^{-1}$ ) for 2014–17 in NAAD HiRes (red), NAAD LoRes (orange), ERA-Interim (blue), ERA5 (cyan), GPCP (green), and GPM (magenta).

diagnostics of ARs (Lavers and Villarini 2015; Ralph et al. 2017; Shields et al. 2018), representing narrow synoptic-scale jets transporting an abundant amount of water vapor from the ocean to the continents. ARs may be responsible for more than 90% of poleward moisture transport (Zhu and Newell 1998) and also result in extreme precipitation events over continental coastal areas (Viale and Nuñez 2011; Lavers and Villarini 2015; Gershunov et al. 2017; Waliser and Guan 2017).

For the detection of ARs, we used the 85th percentile of the integrated water vapor transport (IVT) along with a fixed lower IVT limit of  $100 \text{ kg m}^{-1} \text{ s}^{-1}$  (Guan and Waliser 2015). The 85th percentile of IVT was computed from the 20-day sliding windows in the NAAD-HiRes and LoRes outputs, and moisture transports were computed according to Dufour et al. (2016). Figure 11 shows the case study for 5 December 2015, with an AR associated with the deep cyclone east of Iceland and clearly seen in IVT fields. Associated daily accumulated precipitation in the NAAD HiRes closely matches that diagnosed by GPM, while, for example, ERA-Interim shows the shift in the location of the AR with respect to GPM. NAAD HiRes precipitation in the AR landfall areas over the U.K. and Norway coasts is over  $66 \text{ mm day}^{-1}$ . This is greater than the values diagnosed by NAAD LoRes and ERA-Interim by up to  $30 \text{ mm day}^{-1}$  (Fig. 11f). We also note an accurate location of the coastal precipitation maxima in the landfall areas in NAAD HiRes (Fig. 11f). The maximum of water vapor transport in the AR (Fig. 12a) at 2.5-km height is associated with locally strong winds amounting to more than  $40 \text{ m s}^{-1}$ . Figure 12b shows that the AR core in HiRes is characterized by 10%–15% stronger transports relative to LoRes,

reflecting the fact that ARs in the HiRes experiment are narrower. In climatological context, this reduces the time during which western Europe coasts are exposed to ARs; however, this makes the impact of individual ARs stronger and highly localized. Our estimate for 2015, performed using a method similar to Guan and Waliser (2015), shows that AR landfalls in HiRes happen during 10%–15% of the time, which is less than in LoRes and MERRA (15%–20%).

#### d. Mesoscale features

To demonstrate the representation of mesoscale features in the NAAD, we use kinetic energy (KE) wavenumber spectra (SKE) derived from the wind speed data and averaged over the layer between 3- and 5-km height over the whole domain (Figs. 13a,b). These spectra characterize the atmospheric turbulence at different scales by the power law  $\text{SKE}(k) \sim k^{-\gamma}$ , where  $k$  is the wavenumber and  $\gamma$  is changing from approximately  $-3$  to approximately  $-5/3$  between the ranges of space scales larger and smaller than 500 km (Waite and Snyder 2009; Condon and Renfrew 2013; Dukhovskoy et al. 2017). Figure 13 demonstrates marked differences in the wavenumber spectra for HiRes and LoRes experiments. For the total and geostrophic KE, the HiRes spectrum is better matching  $k^{-3}$  than LoRes is. It is important, however, that the spectral decay rate for both geostrophic and ageostrophic components at smaller scales ( $<500 \text{ km}$ ) is considerably smaller in HiRes than in LoRes. This reflects stronger pressure gradients (and, thus, stronger winds) in synoptic and mesoscale transients in the HiRes experiment. Dukhovskoy et al. (2017) noted a similar tendency in

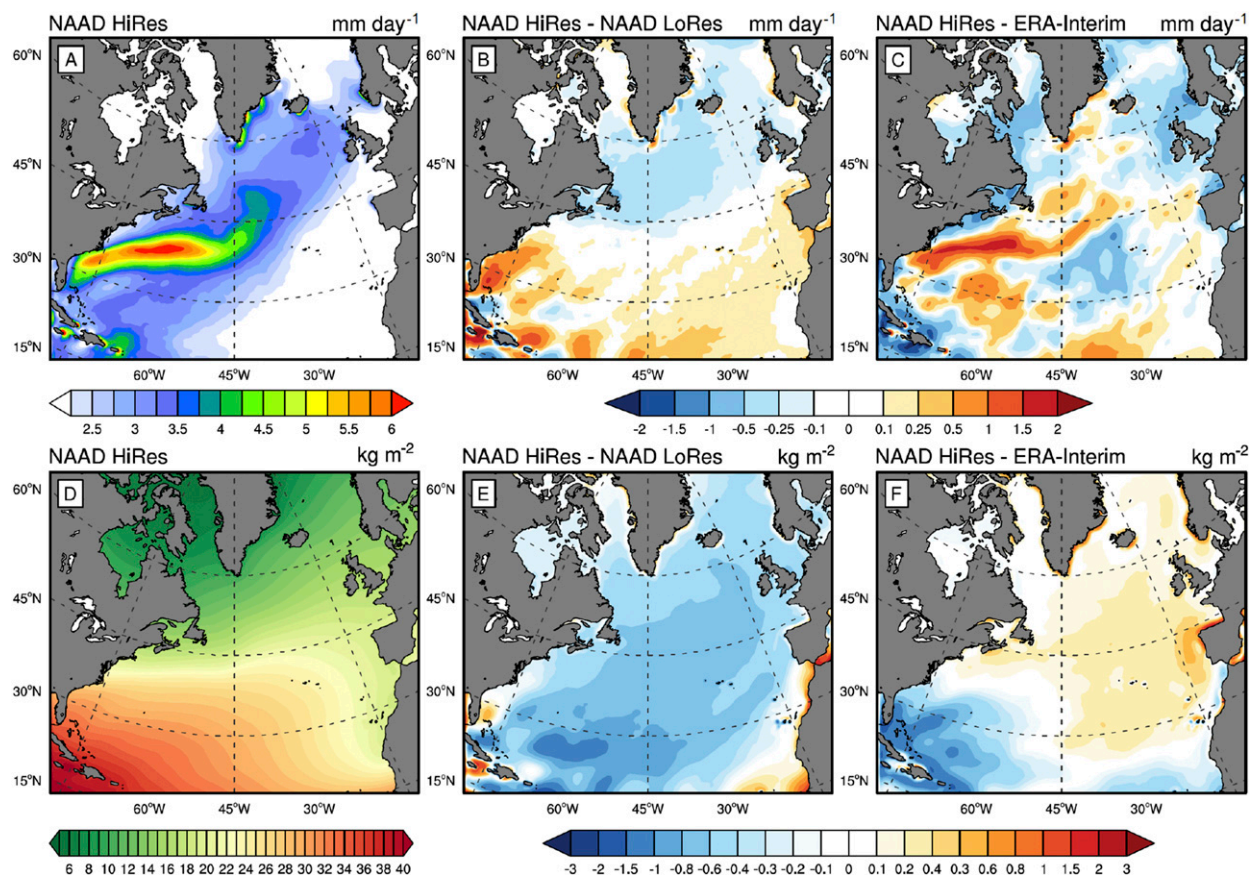


FIG. 9. (a) Annual (1979–2018) mean precipitation ( $\text{mm day}^{-1}$ ) in NAAD HiRes and differences in the annual mean precipitation (b) between NAAD HiRes and NAAD LoRes and (c) between NAAD HiRes and ERA-Interim. Also shown are (d) annual (1979–2018) mean atmospheric precipitable water content ( $\text{kg m}^{-2}$ ) in NAAD HiRes and differences in the annual mean precipitable water content (e) between NAAD HiRes and NAAD LoRes and (f) between NAAD HiRes and ERA-Interim (f).

ASR relative to global coarser-resolution reanalyses in the subpolar North Atlantic.

Figure 13c shows the wavenumber kinetic energy spectra near the surface using data from NAAD HiRes and ASRv2 over the overlapping part of the two domains. As in the case of the free troposphere (Figs. 13a,b), the NAAD HiRes spectrum built from the surface data closely matches  $k^{-5/3}$  decay rate in the range of scales less than 700 km. The ASRv2 spectrum demonstrates a very similar behavior in terms of change in  $\gamma$  from  $\sim -3$  to  $\sim -5/3$  and the decay rate in the range from 700 to at least 100–150 km.

In this respect it is of interest to consider the representation of polar lows in NAAD. Polar lows represent highly localized maritime atmospheric phenomena associated with extreme winds and advection of very dry cold air, playing an important role in high-latitude atmospheric dynamics and air–sea interaction processes (Zahn and von Storch 2008; Condon et al. 2008; Condon and Renfrew 2013, among others). They are

hardly detectable in global reanalyses primarily due to their small size (Zappa et al. 2014; Stoll et al. 2018). Many publications, however, report the capability of the WRF Model even without data assimilation to effectively simulate polar lows (Wagner et al. 2011; Wu et al. 2011; Førre et al. 2012; Kolstad et al. 2016). Kolstad (2011) developed a unique database of 63 polar lows (1999–2009) in the subpolar and subarctic North Atlantic and Arctic using AVHRR and QuikSCAT winds. Of the 21 events identified by Kolstad (2011) in the NAAD domain, NAAD HiRes was able to successfully detect 20 polar lows.

Figure 14 shows a case study for the polar low that developed on 2 March 2008 in the Irminger Sea. NAAD HiRes detects well the location of the pressure minimum identifying a 978-hPa central pressure, which is deeper than that in ERA-Interim (986 hPa) and even in ERA5 (984 hPa). Also, NAAD HiRes demonstrates the well-detectable comma-type structure not present in ERA-Interim and ERA5 and less evident in ASRv2.

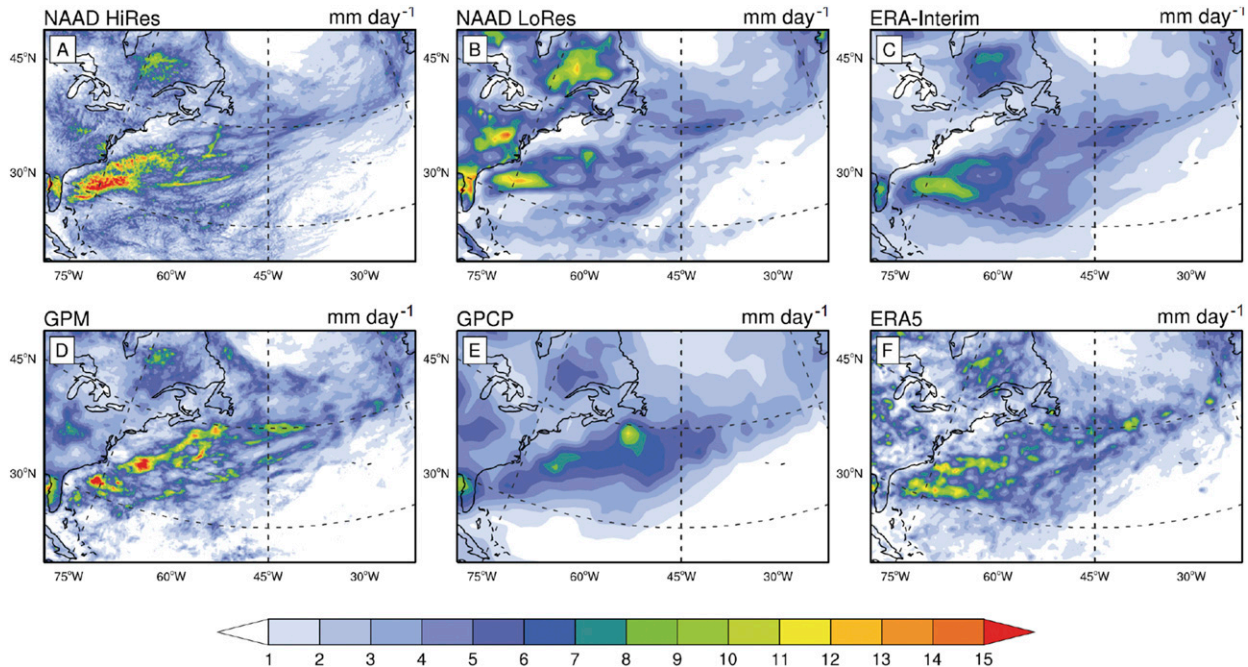


FIG. 10. July 2015 monthly precipitation rates ( $\text{mm day}^{-1}$ ) in (a) NAAD HiRes, (b) LoRes, (c) ERA-Interim, (d) GPM, (e) GPCP, and (f) ERA5.

Note that NAAD LoRes results (no figure shown) are very close to ERA-Interim for this case. The associated maximum surface wind speed in the polar low amounts in HiRes to  $32 \text{ m s}^{-1}$ , with  $26\text{--}27 \text{ m s}^{-1}$  in ERA-Interim and ERA5, and nearly  $30 \text{ m s}^{-1}$  in ASRv2 (Fig. 14). Note that Gutjahr and Heinemann (2018) clearly demonstrated that an accurate representation of the tip jets and associated extreme winds around Greenland requires resolutions of at least 15 km. Remarkably, it is also the case that surface turbulent fluxes (sensible plus latent) are considerably stronger in HiRes (up to  $900 \text{ W m}^{-2}$ ) than in ERA-Interim ( $600 \text{ W m}^{-2}$ ) and are comparable to both ERA5 and ASRv2. We note that the direct comparison of surface fluxes between these products should be taken with caution because of the use of somewhat different flux algorithms. However, the analysis of surface flux PDFs and the surface flux relative extremeness (Gulev and Belyaev 2012; Tilinina et al. 2018) show that the strong flux event during 2 March 2008 in NAAD HiRes contributed more to the total monthly flux as compared with ERA5 and ASRv2.

The capability of the NAAD to capture the mesoscale dynamics in the tropics is evaluated in Fig. 13d showing wavenumber spectra of the kinetic energy near the surface (10 m) and at 1500 m in HiRes and LoRes simulations. Remarkably, the spectra near the surface and at 1500 m are qualitatively close to each other for both simulations and are also close to the spectra for the free

troposphere (Figs. 13a,b) and to the surface spectra in the subpolar region (Fig. 13c). At the same time, tropical spectra for HiRes demonstrate a  $k^{-5/3}$  decay rate for the wave lengths from 200 to 1000 km, while LoRes spectra follow  $k^{-3}$  and a slightly stronger decay rate in this range. This implies more energetic mesoscale features of the same size in the tropics in HiRes than in LoRes.

NAAD is also capable of identifying tropical cyclones generated and propagating north of the southern margin of the domain. Figure 15 shows the diagnostics of Hurricane Gaston, which developed over the North Atlantic between 22 August and 2 September 2016. At the moment of maximum development, NAAD HiRes diagnoses the lowest central pressure (6 hPa deeper when compared with ERA5 and more than 15 hPa deeper than NAAD LoRes and ERA-Interim) as well as winds stronger by  $5\text{--}8 \text{ m s}^{-1}$  than in ERA5. Associated precipitation in NAAD HiRes is considerably stronger than in LoRes and ERA-Interim and consistent in magnitude with ERA5. However, the precipitation pattern in HiRes more accurately captures the shape implied by GPM than ERA5.

## 5. Pilot ocean applications

### a. Effects in modeled ocean circulation

To demonstrate the NAAD capabilities for driving long-term experiments with regional configurations of ocean general circulation models, we developed surface

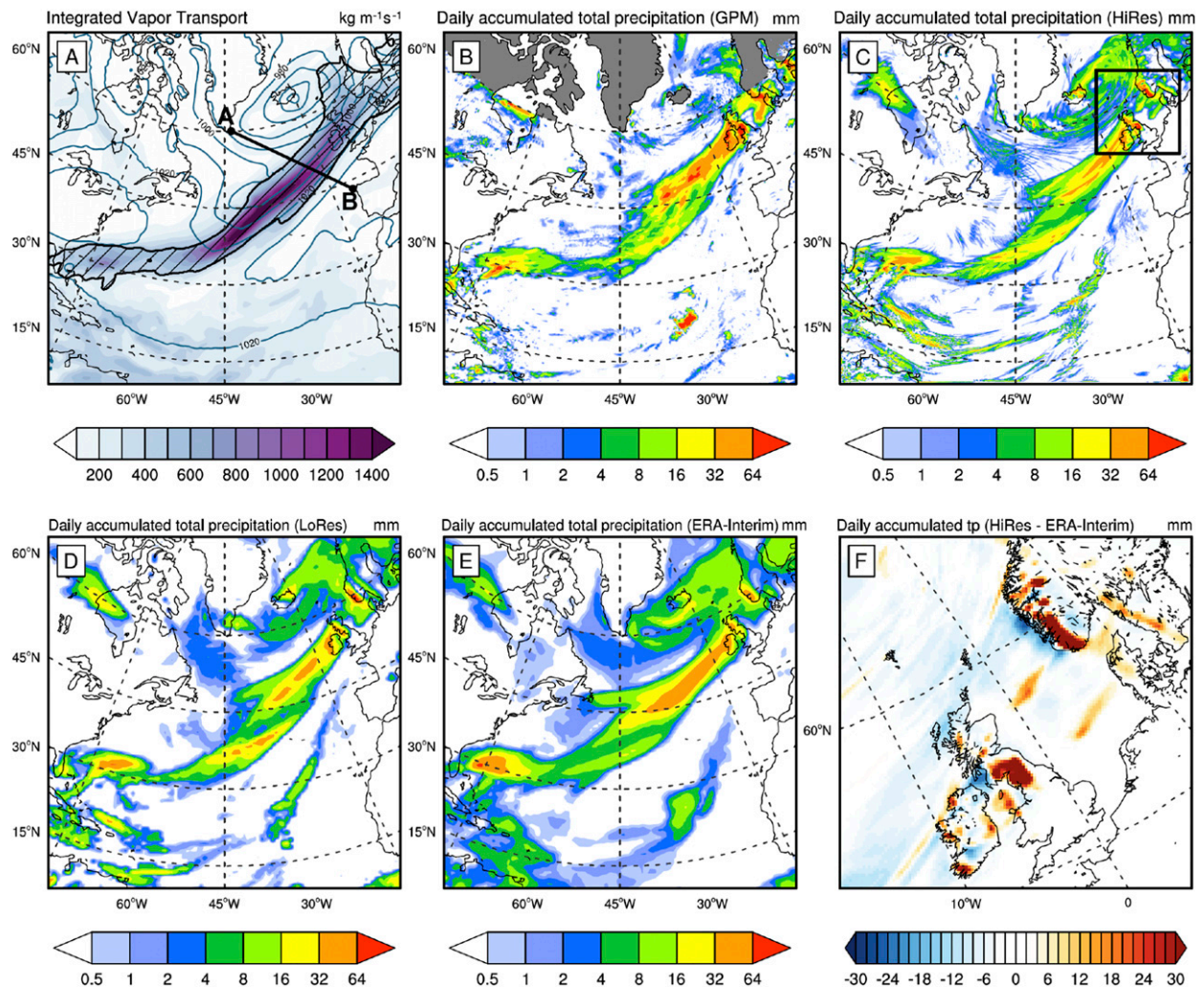


FIG. 11. Representation of AR on 5 Dec 2015: (a) vertically integrated water vapor transport in NAAD HiRes and daily accumulated precipitation diagnosed by (b) GPM, (c) NAAD HiRes, (d) LoRes, and (e) ERA-Interim, along with (f) the difference in precipitation between NAAD HiRes and ERA-Interim over the area of AR landfall. The zoomed-in area in (f) is shown by the black-outlined box in (c). Line AB in (a) shows the cross section displayed in Fig. 12, below.

forcing functions for the ocean based upon NAAD HiRes and NAAD LoRes and used them to drive a northern North Atlantic regional configuration of the NEMO (version 3.6) ocean and sea ice general circulation model (Madec et al. 2016). This configuration (referred to as NNATL12) covers the subpolar gyre of the North Atlantic (Verzemska et al. 2020, manuscript submitted to *J. Geophys. Res.*) at a resolution of approximately 4.5 km. The model configuration setup including configuration geometry ( $1/12^\circ$  grid, 75 vertical  $z$  levels with fine separation (1 m) near the surface, coastlines, and bathymetry), numerical schemes and physical process parameterizations are those commonly used for the global  $1/12^\circ$  eddy-resolving global ocean circulation model ORCA12 for the operational forecasts (Lellouche

et al. 2018) as well as for climate-oriented long-term simulations (e.g., Sérazin et al. 2018; Hewitt et al. 2016) and process studies (e.g., Akuetevi et al. 2016). At the open northern and southern boundaries as well as at the western boundary of Hudson Bay, the model is driven by monthly mean temperature, salinity, velocity, and sea ice from the Global Ocean Reanalysis Simulation (GLORYS12), version 4 (v4) (Garric and Parent 2018). The model was tested in a set of sensitivity experiments and validated against the high-resolution the  $1/12^\circ$  GLORYS12 reanalysis of the Copernicus Marine Environment Monitoring Service (Fernandez and Lellouche 2018), satellite observations, and repeated full-depth hydrographic sections at  $60^\circ\text{N}$  (Sarfanov et al. 2012; Gladyshev et al. 2018;

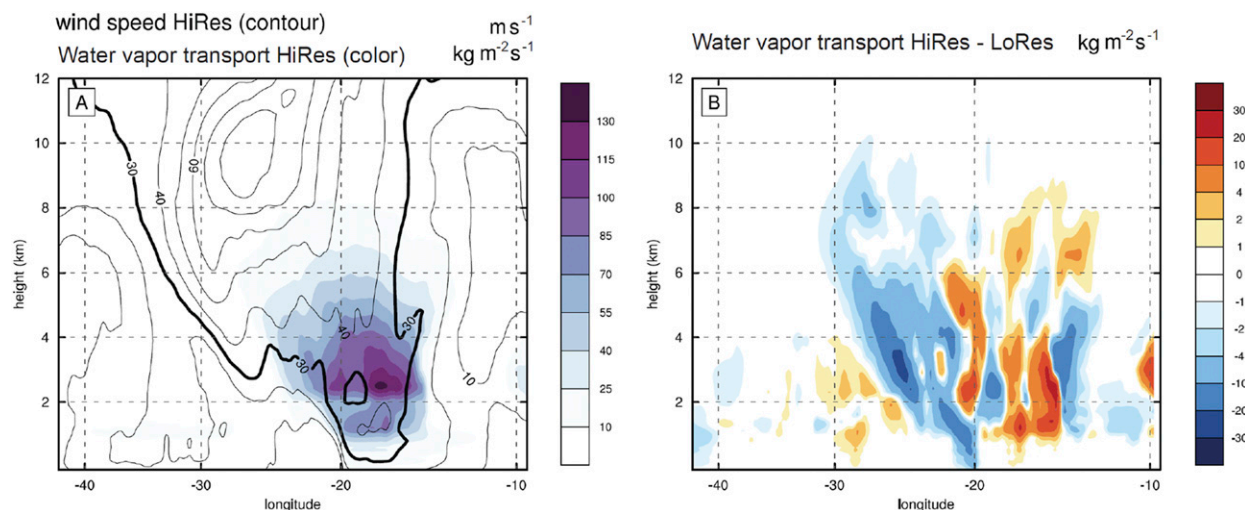


FIG. 12. (a) Moisture transport across the AB section (see Fig. 11a) on 5 Dec 2015 in NAAD HiRes (colors) and the component of wind speed orthogonal to the section (contours) as well as (b) the difference in the moisture transport across the AB section between NAAD HiRes and NAAD LoRes.

Verezemskaya et al. 2020, manuscript submitted to *J. Geophys. Res.*

Comparative model experiments were performed with NAAD HiRes and NAAD LoRes atmospheric forcings; the experiments are referred to as NAAD-OHR and NAAD-OLR, respectively. Significant differences in characteristics of turbulent and radiative heat fluxes as well as momentum fluxes between the two forcings at the ocean surface result in large differences in the simulated ocean mean state. Thus, the domain-averaged simulated SST is approximately 0.6°C lower in NAAD-OHR, with summer differences amounting to more than 1.5°C (Fig. 16), in close agreement with European Space Agency (ESA) SST (<http://www.esa-sst-cci.org>). Note that trends in SST are highly consistent in both NAAD-OHR and NAAD-OLR. The strongest SST negative differences of 1°–1.5°C and lower sea surface salinity (0.15–0.2 psu) in NAAD-OHR relative to NAAD-OLR are observed in the Labrador and Irminger Seas. Consistent with SST, NAAD-OHR shows a lower ocean heat content for both the upper (0–700 m) and intermediate ocean (700–1500 m), suggesting a more intense ventilation of the ocean by convective processes in NAAD-OHR (Fig. 16). Since almost all ocean models in noncoupled experiments have a tendency toward a warmer and saltier ocean (Tréguier et al. 2005; Rattan et al. 2010), the colder upper-ocean temperatures in NAAD-OHR should be considered as an improvement. The OHR forcing also appears to drive significant changes in the boundary currents around Greenland and in the different branches of the central North Atlantic Current, which were found to be more

intense and more variable in NAAD-OHR than in NAAD-OLR, as revealed by the partition of eddy kinetic energy (not shown). NAAD-OHR also shows a somewhat deeper mixed layer depth (MLD) relative to NAAD-OLR (not shown) in regions known for being strongly ventilated by winter convection (the southwest sector of the Labrador Sea and the central Irminger Sea). A lesser ventilation is noticed in the areas where ocean eddies are known to counterbalance the effects of strong surface fluxes onto MLD (e.g., Chanut et al. 2008).

#### b. Effects in ocean wind-wave modeling

NAAD can be also effectively used for forcing spectral wave models whose solutions are critically dependent on the quality and spatial resolution of atmospheric forcing (Cavaleri 2009; Ardhuin et al. 2012). In this respect, the mesoscale activity in the lower atmosphere might be of critical importance for capturing extreme wind waves (Condrón et al. 2006; Zappa et al. 2014; Markina et al. 2019).

We used NAAD HiRes and LoRes outputs for the WAVEWATCH III spectral wave model (WW3DG 2016) over the NAAD domain. Experiments (referred to as NAAD-WHR and NAAD-WLR for HiRes and LoRes forcing, respectively) were performed with the spatial resolution of 0.2° and spectral model resolution being 36 directions and 25 frequencies spanning from 0.04 Hz with an increment of 1.1. The WAVEWATCH-III configuration included ST6 parameterization for wave energy input and dissipation (Zieger et al. 2015; Liu et al. 2019) calibrated for WRF winds (Markina et al. 2018) and the ice source term package (IC0; Tolman

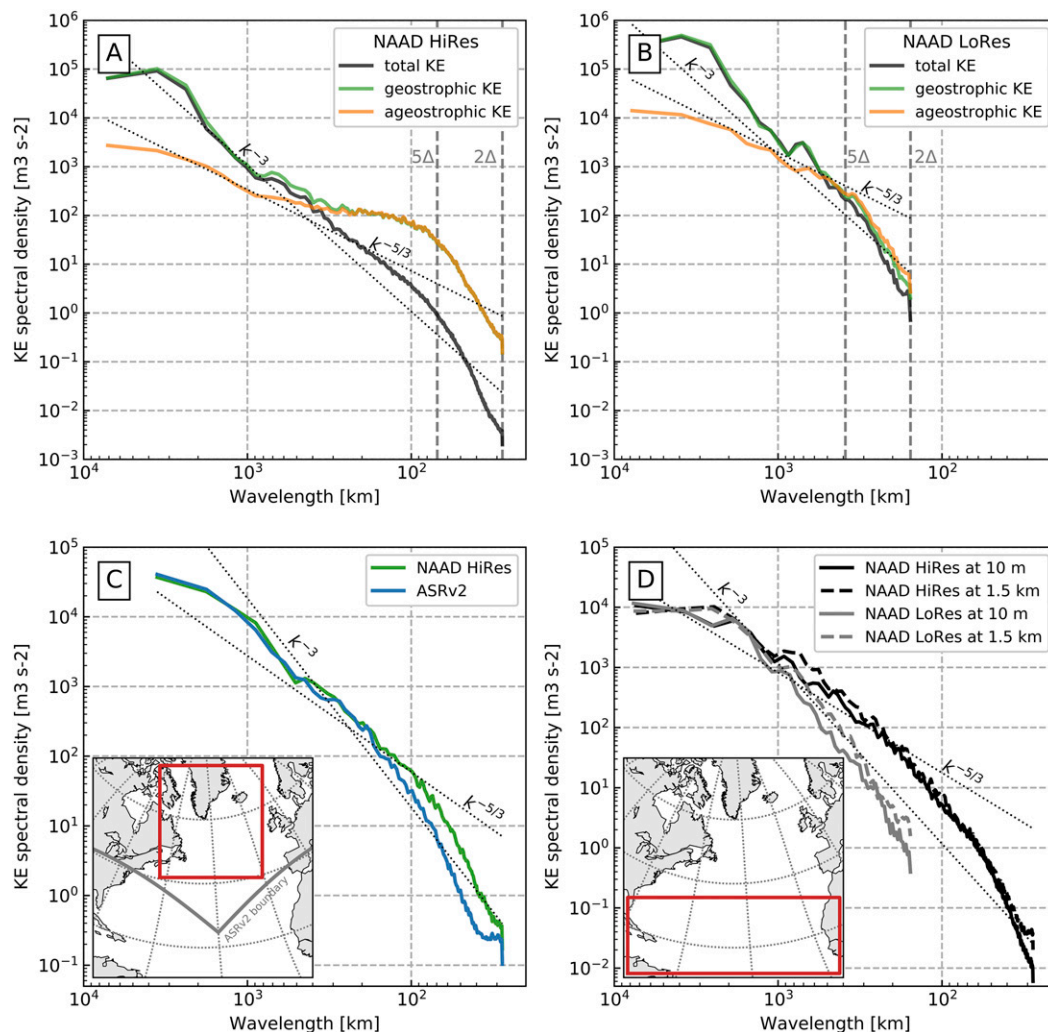


FIG. 13. Wavenumber kinetic energy spectra derived from wind speed data and averaged over the layer between 3- and 5-km height over the whole NAAD domain for (a) NAAD HiRes and (b) NAAD LoRes. In (a) and (b), spectra for the total (black), geostrophic (green), and ageostrophic (yellow) kinetic energy are shown. Dotted lines show power laws of  $k^{-3}$  and  $k^{-5/3}$ , as labeled. (c) Wavenumber kinetic energy spectra derived from surface wind speed diagnosed by NAAD HiRes (green) and ASRv2 (blue) for the area of overlap of the NAAD and ASRv2 domains. The area of overlap of NAAD and ASRv2 is outlined in red in the inlay map, and the gray line in the inlay shows the southern boundary of the ASRv2 domain in the Atlantic region. (d) Wavenumber kinetic energy spectra derived from NAAD HiRes (black) and NAAD LoRes (gray) for the surface (solid lines) and 1500 m (dashed lines) for the tropical domain outlined in red in the inlay map.

2003) implying the exponential attenuation of waves in partially sea ice-covered regions. To account for the ocean surface current impact on growing waves we used daily surface current velocities from the NEMO-based Ocean Reanalysis System 5 (ORAS5; Zuo et al. 2019). Cavaleri (2009) argued that the increase in spatial resolution of forcing per se does not necessarily result in the increase in significant wave height (SWH); rather, the formation of high waves is associated with higher winds, changes in the duration of wind action, and the length of fetch. In this sense, NAAD HiRes with its stronger

winds (Fig. 3), smaller cyclone sizes and larger number of synoptic transients (Figs. 5 and 6) likely acts locally rather than on a larger scale.

Figures 17a and 17b show winter (January–March) climatological SWH for 1979–2018 in NAAD-WHR and the differences between NAAD-WHR and NAAD-WLR. In NAAD-WHR the highest SWH amounts to 5.4 m in the eastern subpolar North Atlantic in very close agreement with VOS observations (Gulev et al. 2003; Gulev and Grigorieva 2006). Differences between NAAD-WHR and NAAD-WLR SWH over most of the

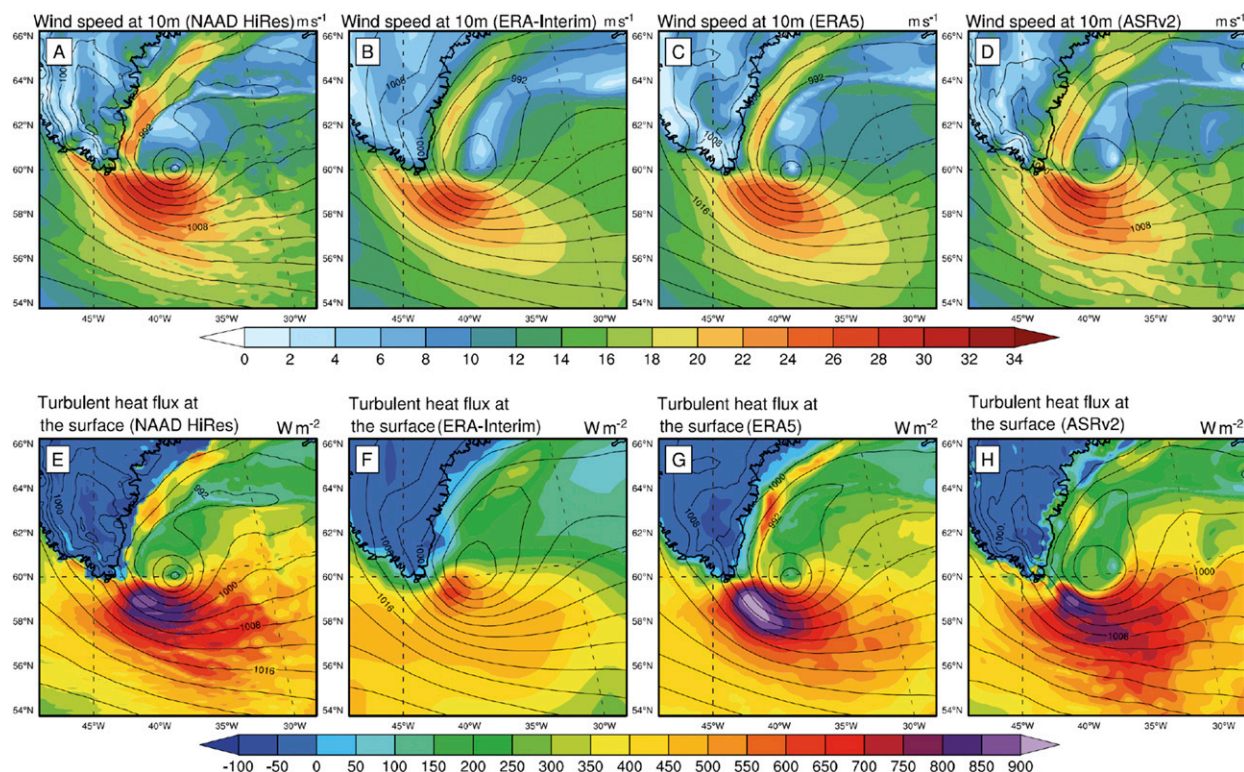


FIG. 14. Diagnostics of the polar low on 2 Mar 2008. Shown is the surface 10-m wind speed (colors) and mean sea level pressure (MSLP; contours) as revealed by (a) NAAD HiRes, (b) ERA-Interim, (c) ERA5, and (d) ASRv2. Also shown is sensible plus latent heat flux (colors) and MSLP (contours) diagnosed by (e) NAAD HiRes, (f) ERA-Interim, (g) ERA5, and (h) ASRv2.

North Atlantic midlatitudes and subtropics are generally within 0.3 m but strongly increase in the subpolar North Atlantic where they amount to 0.8 m in the Irminger Sea. The highest extreme strong waves quantified as 95th percentile amount in winter in NAAD-WHR to 9 m (Fig. 17c), being higher than in NAAD-WLR by 0.2–0.5 m in the central and eastern subpolar North Atlantic (Fig. 17d). At the same time the most distinctive differences between the NAAD-WHR and NAAD-WLR experiments are identified along the southeast Greenland coast where the extreme SWH in NAAD-WHR is higher than that in NAAD-WLR by more than 1 m (up to 20% of mean values). This likely reflects a more accurate representation of katabatic winds and tip jets in this area in NAAD-WHR.

## 6. Summary and outlook

We presented NAAD—a new 3D multidecadal atmospheric dataset for the North Atlantic produced with a WRF nonhydrostatic model at mesoscale resolution (NAAD HiRes). In parallel, a coarser-resolution dataset (NAAD LoRes) was produced with a spatial

resolution close to ERA-Interim used in both experiments as a lateral boundary condition.

Our evaluation demonstrates reasonably realistic representations of most climatological characteristics in both NAAD HiRes and NAAD LoRes datasets. The main differences are identified in the ice-covered subarctic regions, especially for surface air temperature and partly for surface humidity. At the same time, atmospheric dynamics was quite adequately represented. The major purpose of the NAAD at this stage was not to provide extremely close comparability of NAAD LoRes with, for example, ERA-Interim. This is hardly achievable because ERA-Interim (as well as the other reanalyses) is largely constrained by data assimilation. The major NAAD focus was rather to develop a high-resolution atmospheric dataset that allows a better analysis of subsynoptic and mesoscale features—the task still not resolved by global reanalyses over the North Atlantic. In this respect, the objectives for NAAD are similar to those posed for the other regional reanalyses (e.g., ASR; Bromwich et al. 2018). The NAAD model configuration was quite close to the one used in ASR, the lateral conditions are the same (ERA-Interim) and the resolutions of the two products are

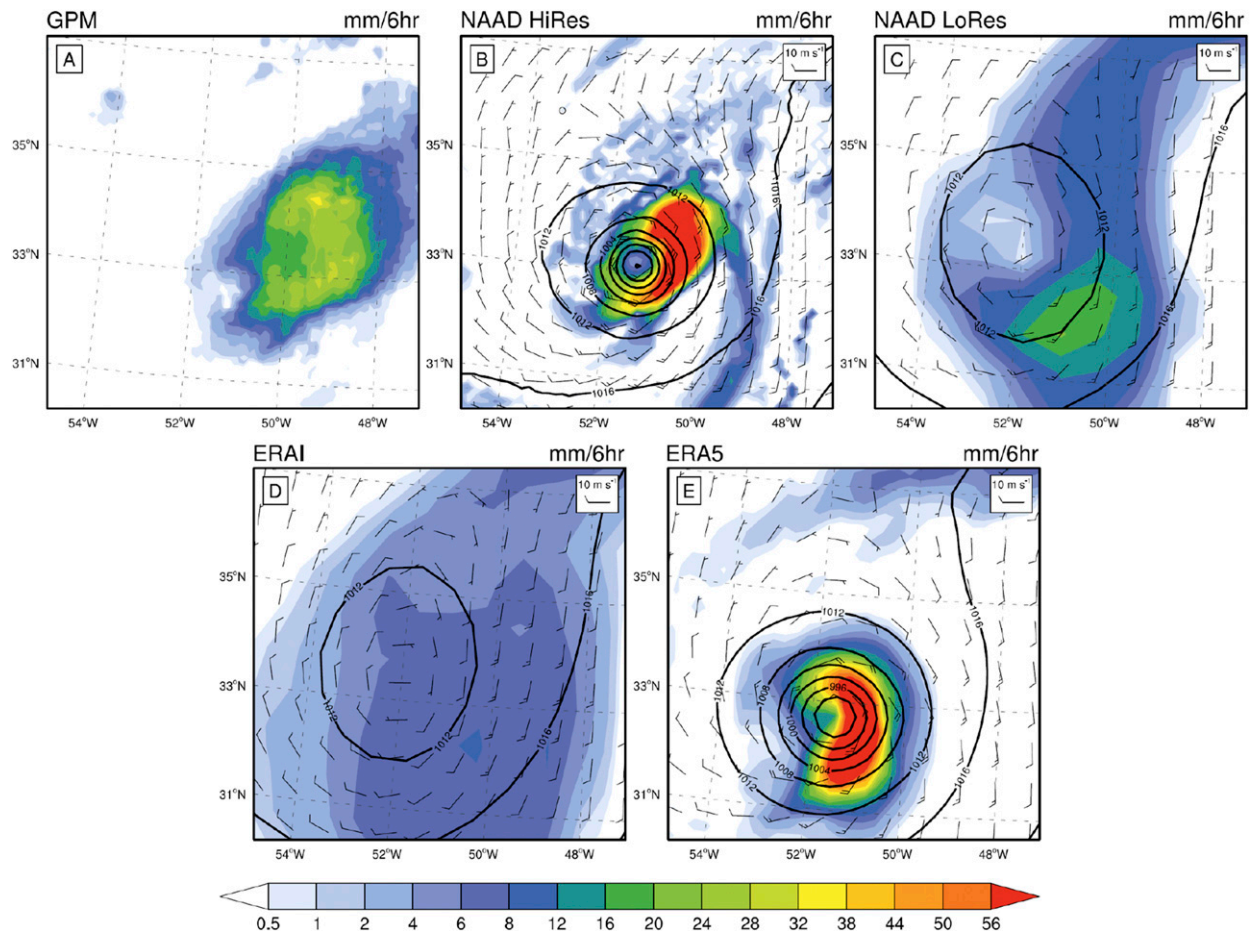


FIG. 15. Diagnostics of Hurricane Gaston in the moment of maximum development on 0000 UTC 31 Aug 2016, showing (a) the precipitation pattern diagnosed by GPM and the MSLP (contours), 10-m wind speed vectors (arrows), and precipitation (colors) as diagnosed by (b) NAAD HiRes, (c) NAAD LoRes, (d) ERA-Interim, and (e) ERA5.

similar. At the same time ASR (both ASRv1 and ASRv2) used extensive data assimilation input that exceeds data assimilation in the global reanalysis (e.g., ERA-Interim). Our capabilities for the direct comparisons of NAAD with ASR were limited to the subpolar latitudes. However, the analysis of kinetic energy spectra and extreme winds and fluxes associated with polar lows (Figs. 13 and 14) clearly demonstrated that the differences between NAAD HiRes and ASRv2 are the smallest relative to the other reanalyses, and this is reassuring. The comparative analysis of surface fluxes, winds, and precipitation in the North Atlantic midlatitudes is not representative, as these regions are close to the boundary of the ASR domain.

Extensive evaluation of ASR (e.g., Moore et al. 2015; Bromwich et al. 2016; Tilinina et al. 2014) demonstrated the added value of high-resolution nonhydrostatic model settings in improving the representation of polar lows and tip jets, as well as extratropical cyclones. In this respect,

our comparison of HiRes and LoRes simulations confirms the conclusions drawn from the ASR evaluation. It also clearly demonstrates the added value of high-resolution and nonhydrostatic model settings in NAAD over the whole North Atlantic. Specifically, NAAD HiRes provides the possibility to resolve mesoscale dynamics associated with high winds, first of all in the North Atlantic subpolar latitudes characterized by small-scale polar lows and tip jets. Here NAAD HiRes demonstrated stronger extreme winds and their better localization compared to the LoRes version and modern reanalyses. Much higher resolution of the WRF Model in NAAD HiRes provides a new view of the North Atlantic extratropical cyclone activity with 2 times as large a total number of cyclones counted in NAAD HiRes relative to LoRes and most reanalyses. This difference was primarily due to cyclones that are smaller in size and relatively shallow, which were poorly simulated in the LoRes experiment and in global reanalyses.

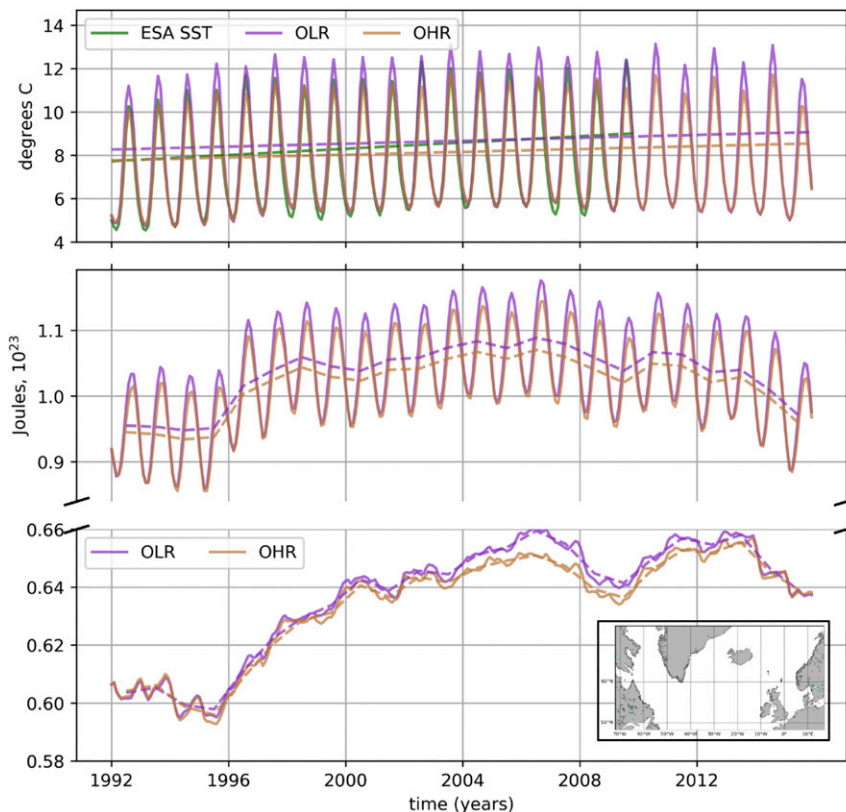


FIG. 16. (top) Domain-averaged simulated ocean SST in NAAD-OHR (orange) and NAAD-OLR (magenta), along with ESA SST (green). Time series of ESA SST are shown only for the period of data availability (1993–2010). (bottom) Domain-averaged ocean heat content for the 0–700-m layer (upper curves) and the 700–1500-m layer (lower curves) in NAAD-OHR (orange) and NAAD-OLR (magenta). The inlay map shows the domain of the NNATL12 ocean general circulation model. Thick lines in the bottom panels show monthly means, and dashed lines show annual means.

Higher extreme turbulent fluxes in NAAD HiRes and a better representation of the convective precipitation over the Gulf Stream make NAAD potentially useful for quantifying ocean–atmosphere interactions at mesoscales and depicting ocean impacts on the lower atmosphere and associated responses in the dynamics of midlatitude storm tracks. NAAD is also capable of capturing highly localized mechanisms of atmospheric moisture transports such as ARs, more accurately locating them, and quantifying their intensity and impacts. In the tropics, NAAD HiRes also effectively captures mesoscale features, including an improved representation of tropical cyclones, especially in terms of central pressure, wind, and precipitation. Applications of NAAD to ocean modeling demonstrated the effect of HiRes onto the modeled ocean state and eddy kinetic energy distribution, specifically showing smaller surface temperature and upper-ocean heat content consistently with observations. Being applied to wind-wave modeling, NAAD

HiRes resulted in higher simulated extreme wind waves in the eastern subpolar North Atlantic, reflecting stronger extremeness of surface winds.

Further near-time developments of the NAAD will include the adaptation of ERA5 as a source for lateral boundary conditions and changing to a finer spatial resolution of at least  $\sim 3$  km with a higher number of vertical layers. This will also include at least for the period after 2000 the use of high-resolution SST and sea ice data, available from the Operational Sea Surface Temperature and Sea Ice Analysis (OSTIA) system (Roberts-Jones et al. 2012; Donlon et al. 2012) as well as from Multisensor Analyzed Sea Ice Extent (MASIE) AMSR2 (MASAM2; Fetterer et al. 2015). Improved representation of sea ice will help to minimize biases in temperature and humidity in the northern North Atlantic. Also planned is the domain extension to the full coverage of the North Atlantic tropics that will make it possible to provide accurate diagnostics of tropical cyclone dynamics including

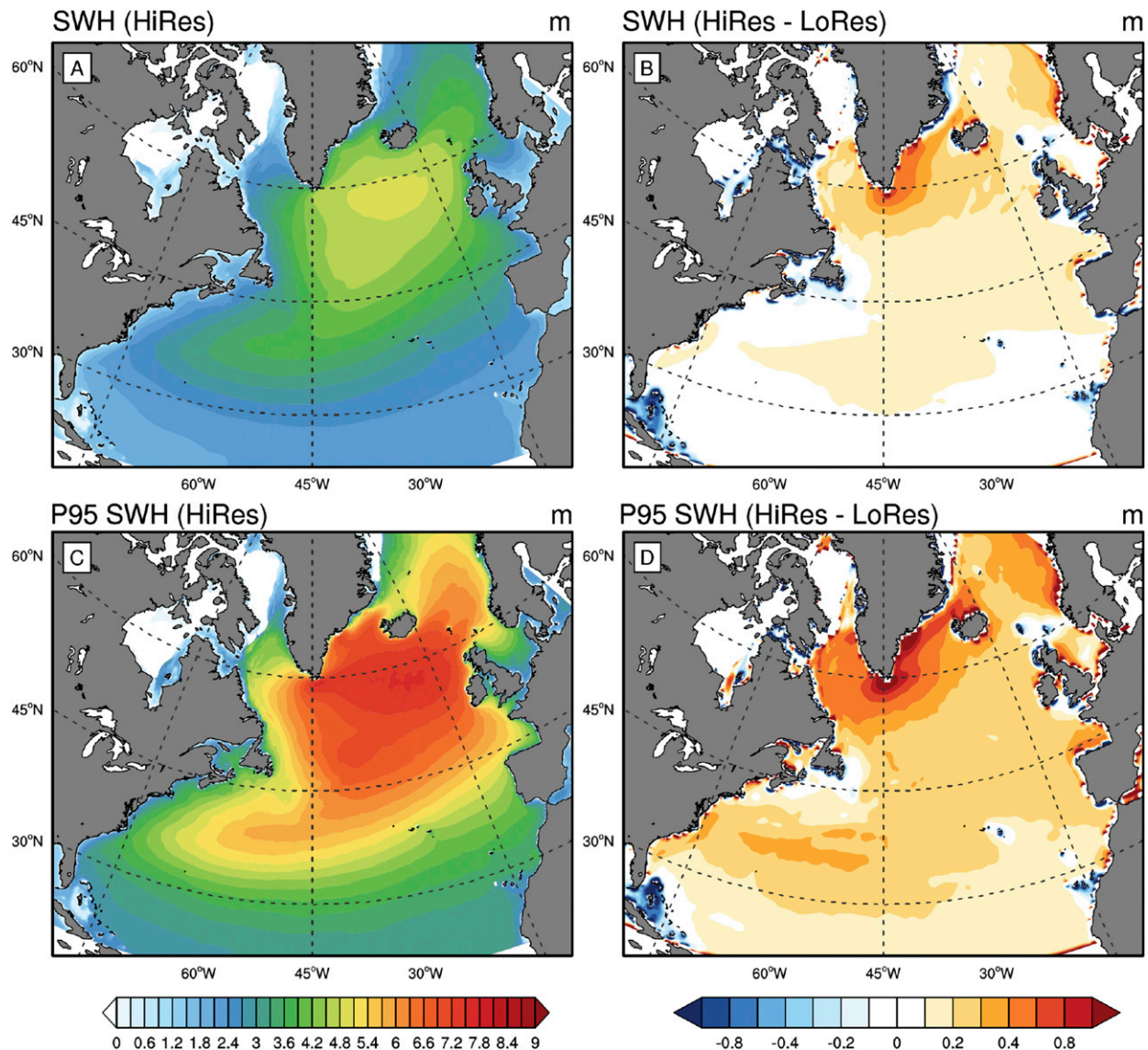


FIG. 17. (a) Mean SWH in NAAD-WHR and (b) difference in the mean SWH between NAAD-WHR and NAAD-WLR over the period of 1979–2018, as well as (c) mean 95th percentile of SWH in NAAD-WHR and (d) difference in 95th percentile of SWH between NAAD-WHR and NAAD-WLR.

the poleward shift in the trajectories (Studholme and Gulev 2018; Sharmila and Walsh 2018). Finer spatial and vertical resolution will also provide a better representation of mesoscale features and will better demonstrate the value added by nonhydrostatic model configurations. For selected years (provisionally in the 2010s), we are also planning to develop ensemble simulations (up to 10 members). In parallel, on a midterm scale we will work on the transition of NAAD to the North Atlantic regional reanalysis with assimilating all available information over the domain that will make it possible to develop the product for assessing the impact of mesoscale processes onto

longer-term climate variability in the atmosphere and the ocean.

*Acknowledgments.* We acknowledge the support by the Russian Academy of Sciences (ST-ASS-0149-2018-0001) and the Ministry of Science and Higher Education of Russian Federation under the Agreement 14.W0331.0006. Authors Tilina and Markina were also supported by Grant 17-77-20112 from the Russian Science Foundation. The analysis of the hydrological cycle (authors Zolina, Dufour, and Krinitskiy) benefited from Helmholtz-RSF Grant 18-47-06202. We greatly appreciate critically important comments of the two anonymous reviewers and

the editor. Their insightful suggestions helped to largely improve the first version of the paper. We thank Peter Koltermann of MSU for useful comments on the paper text. Our analysis of mesoscale dynamics was strongly motivated by Peter Arseev of PhIRAS and Alexey Morozov of ITEP. Discussions on the model setting with Andrey Glazunov of INMRAS are appreciated. We acknowledge the access to the facilities of HPC computing resources at Lomonosov Moscow State University as well as support of the IORAS administration and RSC-Technologies Group in maintaining supercomputers and data storage systems at IORAS.

## REFERENCES

- Akuetevi, C. Q. C., B. Barnier, J. Verron, J.-M. Molines, and A. Lecointre, 2016: Interactions between the Somali current eddies during the summer monsoon: Insights from a numerical study. *Ocean Sci.*, **12**, 185–205, <https://doi.org/10.5194/os-12-185-2016> <https://doi.org/10.5194/OS-12-185-2016>.
- Ardhuin, F., and Coauthors, 2012: Numerical wave modeling in conditions with strong currents: Dissipation, refraction, and relative wind. *J. Phys. Oceanogr.*, **42**, 2101–2120, <https://doi.org/10.1175/JPO-D-11-0220.1>.
- Behrens, E., K. Våge, B. Harden, A. Biastoch, and C. W. Böning, 2017: Composition and variability of the Denmark Strait Overflow Water in a high-resolution numerical model hindcast simulation. *J. Geophys. Res. Oceans*, **122**, 2830–2846, <https://doi.org/10.1002/2016JC012158>.
- Bentamy, A., and Coauthors, 2017: Review and assessment of latent and sensible heat flux accuracy over the global oceans. *Remote Sens. Environ.*, **201**, 196–218, <https://doi.org/10.1016/j.rse.2017.08.016> <https://doi.org/10.1016/J.RSE.2017.08.016>.
- Bishop, S. P., R. J. Small, F. O. Bryan, and R. A. Tomas, 2017: Scale dependence of midlatitude air–sea interaction. *J. Climate*, **30**, 8207–8221, <https://doi.org/10.1175/JCLI-D-17-0159.1>.
- Boisvert, L. N., M. A. Webster, A. A. Petty, T. Markus, D. H. Bromwich, and R. I. Cullather, 2018: Intercomparison of precipitation estimates over the Arctic Ocean and its peripheral seas from reanalyses. *J. Climate*, **31**, 8441–8462, <https://doi.org/10.1175/JCLI-D-18-0125.1>.
- Bond, N. A., and M. F. Cronin, 2008: Regional weather patterns during anomalous air–sea fluxes at the Kuroshio Extension Observatory (KEO). *J. Climate*, **21**, 1680–1697, <https://doi.org/10.1175/2007JCLI1797.1>.
- Brodeau, L., B. Barnier, A.-M. Treguier, T. Penduff, and S. Gulev, 2010: An ERA40-based atmospheric forcing for global ocean circulation models. *Ocean Modell.*, **31**, 88–104, <https://doi.org/10.1016/j.ocemod.2009.10.005>.
- , —, S. K. Gulev, and C. Woods, 2017: Climatologically significant effects of some approximations in the bulk parameterizations of turbulent air–sea fluxes. *J. Phys. Oceanogr.*, **47**, 5–28, <https://doi.org/10.1175/JPO-D-16-0169.1>.
- Bromwich, D. H., K. M. Hines, and L.-S. Bai, 2009: Development and testing of Polar Weather Research and Forecasting model: 2. Arctic Ocean. *J. Geophys. Res.*, **114**, D08122, <https://doi.org/10.1029/2008JD010300>.
- , A. B. Wilson, L. Bai, G. W. Moore, and P. Bauer, 2016: A comparison of the regional Arctic System Reanalysis and the global ERA-Interim reanalysis for the Arctic. *Quart. J. Roy. Meteor. Soc.*, **142**, 644–658, <https://doi.org/10.1002/qj.2527> <https://doi.org/10.1002/QJ.2527>.
- , and Coauthors, 2018: The Arctic System Reanalysis, version 2. *Bull. Amer. Meteor. Soc.*, **99**, 805–828, <https://doi.org/10.1175/BAMS-D-16-0215.1>.
- Bukovsky, M. S., and D. J. Karoly, 2009: Precipitation simulations using WRF as a nested regional climate model. *J. Appl. Meteor. Climatol.*, **48**, 2152–2159, <https://doi.org/10.1175/2009JAMC2186.1>.
- Cavaleri, L., 2009: Wave modeling—Missing the peaks. *J. Phys. Oceanogr.*, **39**, 2757–2778, <https://doi.org/10.1175/2009JPO4067.1>.
- Chanut, J., B. Barnier, W. Large, L. Debreu, T. Penduff, J.-M. Molines, and P. Mathiot, 2008: Mesoscale eddies in the Labrador Sea and their contribution to convection and restratification. *J. Phys. Oceanogr.*, **38**, 1617–1643, <https://doi.org/10.1175/2008JPO3485.1>.
- Chao, Y., Z. Li, J. D. Farrara, and P. Hung, 2009: Blending sea surface temperatures from multiple satellites and in situ observations for coastal oceans. *J. Atmos. Oceanic Technol.*, **26**, 1415–1426, <https://doi.org/10.1175/2009JTECHO592.1>.
- Chassignet, E. P., and X. Xu, 2017: Impact of horizontal resolution (1/12° to 1/50°) on Gulf Stream separation, penetration, and variability. *J. Phys. Oceanogr.*, **47**, 1999–2021, <https://doi.org/10.1175/JPO-D-17-0031.1>.
- Chelton, D. B., and F. J. Wentz, 2005: Global microwave satellite observations of sea surface temperature for numerical weather prediction and climate research. *Bull. Amer. Meteor. Soc.*, **86**, 1097–1116, <https://doi.org/10.1175/BAMS-86-8-1097>.
- Chen, F., and J. Dudhia, 2001: Coupling an advanced land surface–hydrology model with the Penn State–NCAR MM5 modeling system. Part I: Model implementation and sensitivity. *Mon. Wea. Rev.*, **129**, 569–585, [https://doi.org/10.1175/1520-0493\(2001\)129<0569:CAALSH>2.0.CO;2](https://doi.org/10.1175/1520-0493(2001)129<0569:CAALSH>2.0.CO;2).
- Condron, A., and I. A. Renfrew, 2013: The impact of polar mesoscale storms on northeast Atlantic Ocean circulation. *Nat. Geosci.*, **6**, 34–37, <https://doi.org/10.1038/ngeo1661> <https://doi.org/10.1038/NGEO1661>.
- , G. R. Bigg, and I. Renfrew, 2006: Polar mesoscale cyclones in the northeast Atlantic: Comparing climatologies from ERA-40 and satellite imagery. *Mon. Wea. Rev.*, **134**, 1518–1533, <https://doi.org/10.1175/MWR3136.1>.
- , —, and I. A. Renfrew, 2008: Modeling the impact of polar mesocyclones on ocean circulation. *J. Geophys. Res. Oceans*, **113**, C10005, <https://doi.org/10.1029/2007JC004599>.
- Copernicus Climate Change Service, 2017: ERA5 hourly data on single levels from 1979 to present. Copernicus Climate Change Service Climate Data Store, accessed 23 August 2019, <https://doi.org/10.24381/cds.adbb2d47>.
- Danabasoglu, G., and Coauthors, 2014: North Atlantic simulations in Coordinated Ocean–Ice Reference Experiments phase II (CORE-II). Part I: Mean states. *Ocean Modell.*, **73**, 76–107, <https://doi.org/10.1016/j.ocemod.2013.10.005> <https://doi.org/10.1016/J.OCEMOD.2013.10.005>.
- , and Coauthors, 2016: North Atlantic simulations in Coordinated Ocean–Ice Reference Experiments phase II (CORE-II). Part II: Inter-annual to decadal variability. *Ocean Modell.*, **97**, 65–90, <https://doi.org/10.1016/j.ocemod.2015.11.007> <https://doi.org/10.1016/J.OCEMOD.2015.11.007>.
- Dee, D. P., and Coauthors, 2011: The ERA-Interim reanalysis: Configuration and performance of the data assimilation system. *Quart. J. Roy. Meteor. Soc.*, **137**, 553–597, <https://doi.org/10.1002/qj.828> <https://doi.org/10.1002/QJ.828>.

- Deshayes, J., and Coauthors, 2013: Oceanic hindcast simulations at high resolution suggest that the Atlantic MOC is bistable. *Geophys. Res. Lett.*, **40**, 3069–3073, <https://doi.org/10.1002/grl.50534> <https://doi.org/10.1002/GRL.50534>.
- Donlon, C., M. Martin, J. Stark, J. Roberts-Jones, E. Fiedler, and W. Wimmer, 2012: The Operational Sea Surface Temperature and Sea Ice Analysis (OSTIA) system. *Remote Sens. Environ.*, **116**, 140–158, <https://doi.org/10.1016/j.rse.2010.10.017> <https://doi.org/10.1016/J.RSE.2010.10.017>.
- Dufour, A., O. Zolina, and S. K. Gulev, 2016: Atmospheric moisture transport to the Arctic: Assessment of reanalyses and analysis of transport components. *J. Climate*, **29**, 5061–5081, <https://doi.org/10.1175/JCLI-D-15-0559.1>.
- Dukhovskoy, D. S., M. A. Bourassa, G. N. Petersen, and J. Steffen, 2017: Comparison of the ocean surface vector winds from atmospheric reanalysis and scatterometer-based wind products over the Nordic Seas and the northern North Atlantic and their application for ocean modeling. *J. Geophys. Res. Oceans*, **122**, 1943–1973, <https://doi.org/10.1002/2016JC012453>.
- DuVivier, A. K., J. J. Cassano, A. Craig, J. Hamman, W. Maslowski, B. Nijssen, R. Osinski, and A. Roberts, 2016: Winter atmospheric buoyancy forcing and oceanic response during strong wind events around southeastern Greenland in the Regional Arctic System Model (RASAM) for 1990–2010. *J. Climate*, **29**, 975–994, <https://doi.org/10.1175/JCLI-D-15-0592.1>.
- Fairall, C. W., E. F. Bradley, J. E. Hare, A. A. Grachev, and J. B. Edson, 2003: Bulk parameterization of air–sea fluxes: Updates and verification for the COARE algorithm. *J. Climate*, **16**, 571–591, [https://doi.org/10.1175/1520-0442\(2003\)016<0571:BPOASF>2.0.CO;2](https://doi.org/10.1175/1520-0442(2003)016<0571:BPOASF>2.0.CO;2).
- Fallmann, J., H. Lewis, J. C. Sanchez, and A. Lock, 2019: Impact of high-resolution ocean–atmosphere coupling on fog formation over the North Sea. *Quart. J. Roy. Meteor. Soc.*, **145**, 1180–1201, <https://doi.org/10.1002/qj.3488> <https://doi.org/10.1002/QJ.3488>.
- Fernandez, E., and J.-M. Lellouche, 2018: Product user manual for the Global Ocean Physical Reanalysis product: GLOBAL\_REANALYSIS\_PHY\_001\_030. CMEMS Rep. CMEMS-GLO-PUM-001-030, 15 pp., <http://cmems-resources.cls.fr/documents/PUM/CMEMS-GLO-PUM-001-030.pdf>.
- Fetterer, F., J. S. Stewart, and W. N. Meier, 2015: MASAM2: Daily 4 km Arctic sea ice concentration, version 1. National Snow and Ice Data Center, accessed 23 August 2019, <https://doi.org/10.7265/N5ZS2TFT>.
- Føre, I., J. E. Kristjánsson, E. W. Kolstad, T. J. Bracegirdle, Ø. Saetra, and B. Røsting, 2012: A ‘hurricane-like’ polar low fuelled by sensible heat flux: High-resolution numerical simulations. *Quart. J. Roy. Meteor. Soc.*, **138**, 1308–1324, <https://doi.org/10.1002/qj.1876> <https://doi.org/10.1002/QJ.1876>.
- Fresnay, S., A. L. Ponte, S. Le Gentil, and J. Le Sommer, 2018: Reconstruction of the 3-D dynamics from surface variables in a high-resolution simulation of North Atlantic. *J. Geophys. Res. Oceans*, **123**, 1612–1630, <https://doi.org/10.1002/2017JC013400>.
- Gao, Y., J. Xu, and D. Chen, 2015: Evaluation of WRF mesoscale climate simulations over the Tibetan Plateau during 1979–2011. *J. Climate*, **28**, 2823–2841, <https://doi.org/10.1175/JCLI-D-14-00300.1>.
- Garric, G., and L. Parent, 2018: Product user manual for Global Ocean Reanalysis product: GLOBAL-REANALYSIS-PHY-001-025. CMEMS Rep. CMEMS-GLO-PUM-001-025, 19 pp., <http://resources.marine.copernicus.eu/documents/PUM/CMEMS-GLO-PUM-001-025.pdf>.
- Gelaro, R., and Coauthors, 2017: The Modern-Era Retrospective Analysis for Research and Applications, version 2 (MERRA-2). *J. Climate*, **30**, 5419–5454, <https://doi.org/10.1175/JCLI-D-16-0758.1>.
- Gershunov, A., T. Shulgina, F. M. Ralph, D. A. Lavers, and J. J. Rutz, 2017: Assessing the climate-scale variability of atmospheric rivers affecting western North America. *Geophys. Res. Lett.*, **44**, 7900–7908, <https://doi.org/10.1002/2017GL074175>.
- Gimeno, L., R. Nieto, M. Vázquez, and D. Lavers, 2014: Atmospheric rivers: A mini-review. *Front. Earth Sci.*, **2**, 2296–6463, <https://doi.org/10.3389/feart.2014.00002> <https://doi.org/10.3389/FEART.2014.00002>.
- Gladyshev, S. V., V. S. Gladyshev, S. K. Gulev, and A. Sokov, 2018: Structure and variability of the meridional overturning circulation in the North Atlantic Subpolar Gyre, 2007–2017. *Dokl. Earth Sci.*, **483**, 1524–1527, <https://doi.org/10.1134/S1028334X18120024>.
- Guan, B., and D. E. Waliser, 2015: Detection of atmospheric rivers: Evaluation and application of an algorithm for global studies. *J. Geophys. Res. Atmos.*, **120**, 12 514–12 535, <https://doi.org/10.1002/2015JD024257>.
- Gulev, S. K., and V. Grigorieva, 2006: Variability of the winter wind waves and swell in the North Atlantic and North Pacific as revealed by the voluntary observing ship data. *J. Climate*, **19**, 5667–5685, <https://doi.org/10.1175/JCLI3936.1>.
- , and K. Belyaev, 2012: Probability distribution characteristics for surface air–sea turbulent heat fluxes over the global ocean. *J. Climate*, **25**, 184–206, <https://doi.org/10.1175/2011JCLI4211.1>.
- , V. Grigorieva, A. Sterl, and D. Woolf, 2003: Assessment of the reliability of wave observations from voluntary observing ships: Insights from the validation of a global wind wave climatology based on voluntary observing ship data. *J. Geophys. Res.*, **108**, 3236, <https://doi.org/10.1029/2002JC001437>.
- Guo, C., M. Ilicak, I. Fer, E. Darelius, and M. Bentsen, 2014: Baroclinic instability of the Faroe Bank Channel Overflow. *J. Phys. Oceanogr.*, **44**, 2698–2717, <https://doi.org/10.1175/JPO-D-14-0080.1>.
- Gutjahr, O., and G. Heinemann, 2018: A model-based comparison of extreme winds in the Arctic and around Greenland. *Int. J. Climatol.*, **38**, 5272–5292, <https://doi.org/10.1002/joc.5729> <https://doi.org/10.1002/JOC.5729>.
- Hand, R., N. Keenlyside, N.-E. Omrani, and M. Latif, 2014: Simulated response to inter-annual SST variations in the Gulf Stream region. *Climate Dyn.*, **42**, 715–731, <https://doi.org/10.1007/s00382-013-1715-y> <https://doi.org/10.1007/S00382-013-1715-Y>.
- Hanley, K. E., S. E. Belcher, and P. P. Sullivan, 2010: A global climatology of wind–wave interaction. *J. Phys. Oceanogr.*, **40**, 1263–1282, <https://doi.org/10.1175/2010JPO4377.1>.
- Hewitt, H. T., and Coauthors, 2016: The impact of resolving the Rossby radius at mid-latitudes in the ocean: Results from a high-resolution version of the Met Office GC2 coupled model. *Geosci. Model Dev.*, **9**, 3655–3670, <https://doi.org/10.5194/gmd-9-3655-2016>.
- Hong, S.-Y., and J.-O. J. Lim, 2006: The WRF single-moment 6-class microphysics scheme (WSM6). *J. Korean Meteor. Soc.*, **42**, 129–151.
- , J. Dudhia, and S.-H. Chen, 2004: A revised approach to ice microphysical processes for the bulk parameterization of clouds and precipitation. *Mon. Wea. Rev.*, **132**, 103–120, [https://doi.org/10.1175/1520-0493\(2004\)132<0103:ARATIM>2.0.CO;2](https://doi.org/10.1175/1520-0493(2004)132<0103:ARATIM>2.0.CO;2).

- , Y. Noh, and J. Dudhia, 2006: A new vertical diffusion package with an explicit treatment of entrainment processes. *Mon. Wea. Rev.*, **134**, 2318–2341, <https://doi.org/10.1175/MWR3199.1>.
- Huffman, G. J., R. F. Adler, M. M. Morrissey, D. T. Bolvin, S. Curtis, R. Joyce, B. McGavock, and J. Susskind, 2001: Global precipitation at one-degree daily resolution from multisatellite observations. *J. Hydrometeorol.*, **2**, 36–50, [https://doi.org/10.1175/1525-7541\(2001\)002<0036:GPAODD>2.0.CO;2](https://doi.org/10.1175/1525-7541(2001)002<0036:GPAODD>2.0.CO;2).
- Iacono, M. J., J. S. Delamere, E. J. Mlawer, M. W. Shepard, S. A. Clough, and W. D. Collins, 2008: Radiative forcing by long-lived greenhouse gases: Calculations with the AER radiative transfer models. *J. Geophys. Res.*, **113**, D13103, <https://doi.org/10.1029/2008JD009944>.
- Jeuken, A. B. M., P. C. Siegmund, L. C. Heijboer, J. Feichter, and L. Bengtsson, 1996: On the potential of assimilating meteorological analyses in a global climate model for the purpose of model validation. *J. Geophys. Res.*, **101**, 16 939–16 950, <https://doi.org/10.1029/96JD01218>.
- Justino, F., A. B. Wilson, D. H. Bromwich, A. Avila, L.-S. Bai, and S.-H. Wang, 2019: Northern Hemisphere extratropical turbulent heat fluxes in ASRv2 and global reanalyses. *J. Climate*, **32**, 2145–2166, <https://doi.org/10.1175/JCLI-D-18-0535.1>.
- Kain, J. S., 2004: The Kain–Fritsch convective parameterization: An update. *J. Appl. Meteor.*, **43**, 170–181, [https://doi.org/10.1175/1520-0450\(2004\)043<0170:TKCPAU>2.0.CO;2](https://doi.org/10.1175/1520-0450(2004)043<0170:TKCPAU>2.0.CO;2).
- Kim, W. M., S. Yeager, P. Chang, and G. Danabasoglu, 2016: Atmospheric conditions associated with Labrador Sea deep convection: New insights from a case study of the 2006/07 and 2007/08 winters. *J. Climate*, **29**, 5281–5297, <https://doi.org/10.1175/JCLI-D-15-0527.1>.
- Kobayashi, S., and Coauthors, 2015: The JRA-55 Reanalysis: General specifications and basic characteristics. *J. Meteor. Soc. Japan Ser. II*, **93**, 5–48, <https://doi.org/10.2151/jmsj.2015-001> <https://doi.org/10.2151/JMSJ.2015-001>.
- Kolstad, E. W., 2011: A global climatology of favourable conditions for polar lows. *Quart. J. Roy. Meteor. Soc.*, **137**, 1749–1761, <https://doi.org/10.1002/qj.888> <https://doi.org/10.1002/QJ.888>.
- , T. J. Bracegirdle, and M. Zahn, 2016: Re-examining the roles of surface heat flux and latent heat release in a “hurricane-like” polar low over the Barents Sea. *J. Geophys. Res. Atmos.*, **121**, 7853–7867, <https://doi.org/10.1002/2015JD024633>.
- Kumar, A., L. Zhang, and W. Wang, 2013: Sea surface temperature–precipitation relationship in different reanalyses. *Mon. Wea. Rev.*, **141**, 1118–1123, <https://doi.org/10.1175/MWR-D-12-00214.1>.
- Large, W. G., and S. G. Yeager, 2004: Diurnal to decadal global forcing for ocean and sea-ice models: The data sets and flux climatologies. NCAR Tech. Note NCAR/TN-460+STR, 105 pp., <https://doi.org/10.5065/D6KK98Q6>.
- , and —, 2009: The global climatology of an interannually varying air–sea flux data set. *Climate Dyn.*, **33**, 341–364, <https://doi.org/10.1007/s00382-008-0441-3> <https://doi.org/10.1007/S00382-008-0441-3>.
- Lavers, D. A., and G. Villarini, 2015: The contribution of atmospheric rivers to precipitation in Europe and the United States. *J. Hydrol.*, **522**, 382–390, <https://doi.org/10.1016/j.jhydrol.2014.12.010> <https://doi.org/10.1016/J.JHYDROL.2014.12.010>.
- , R. P. Allan, E. F. Wood, G. Villarini, D. J. Brayshaw, and A. J. Wade, 2011: Winter floods in Britain are connected to atmospheric rivers. *Geophys. Res. Lett.*, **38**, L23803, <https://doi.org/10.1029/2011GL049783>.
- Lellouche, J.-M., and Coauthors, 2018: The Mercator Ocean global high-resolution monitoring and forecasting system. *New Frontiers in Operational Oceanography*, E. Chassignet, Eds., GODAE OceanView, 563–592.
- Liu, Q., W. E. Rogers, A. V. Babanin, I. R. Young, L. Romero, S. Zieger, F. Qiao, and C. Guan, 2019: Observation-based source terms in the third-generation wave model WAVEWATCH III: Updates and verification. *J. Phys. Oceanogr.*, **49**, 489–517, <https://doi.org/10.1175/JPO-D-18-0137.1>.
- Ma, X., P. Chang, R. Saravanan, D. Wu, X. Lin, L. Wu, and X. Wan, 2015: Winter extreme flux events in the Kuroshio and Gulf Stream extension regions and relationship with modes of North Pacific and Atlantic variability. *J. Climate*, **28**, 4950–4970, <https://doi.org/10.1175/JCLI-D-14-00642.1>.
- , —, —, R. Montuoro, H. Nakamura, D. Wu, X. Lin, and L. Wu, 2017: Importance of resolving Kuroshio front and eddy influence in simulating the North Pacific storm track. *J. Climate*, **30**, 1861–1880, <https://doi.org/10.1175/JCLI-D-16-0154.1>.
- Madec, G., and Coauthors, 2016: NEMO ocean engine. Institut Pierre-Simon Laplace Note du Pôle de Modélisation 27, 396 pp., [https://www.nemo-ocean.eu/wp-content/uploads/NEMO\\_book.pdf](https://www.nemo-ocean.eu/wp-content/uploads/NEMO_book.pdf).
- Markina, M., A. Gavrikov, S. Gulev, and B. Barnier, 2018: Developing configuration of WRF model for long-term high-resolution wind wave hindcast over the North Atlantic with WAVEWATCH III. *Ocean Dyn.*, **68**, 1593–1604, <https://doi.org/10.1007/s10236-018-1215-z> <https://doi.org/10.1007/S10236-018-1215-Z>.
- , J. H. P. Studholme, and S. K. Gulev, 2019: Ocean wind wave climate responses to wintertime North Atlantic atmospheric transient eddies and low-frequency flow. *J. Climate*, **32**, 5619–5638, <https://doi.org/10.1175/JCLI-D-18-0595.1>.
- Miguez-Macho, G., G. L. Stenchikov, and A. Robock, 2004: Spectral nudging to eliminate the effects of domain position and geometry in regional climate model simulations. *J. Geophys. Res.*, **109**, D13104, <https://doi.org/10.1029/2003JD004495>.
- Minobe, S., A. Kuwano-Yoshida, N. Komori, S.-P. Xie, and R. J. Small, 2008: Influence of the Gulf Stream on the troposphere. *Nature*, **452**, 206–209, <https://doi.org/10.1038/nature06690> <https://doi.org/10.1038/NATURE06690>.
- , M. Miyashita, A. Kuwano-Yoshida, H. Tokinaga, and S.-P. Xie, 2010: Atmospheric response to the Gulf Stream: Seasonal variations. *J. Climate*, **23**, 3699–3719, <https://doi.org/10.1175/2010JCLI3359.1>.
- Moore, G. W. K., and I. A. Renfrew, 2005: Tip jets and barrier winds: A QuikSCAT climatology of high wind speed events around Greenland. *J. Climate*, **18**, 3713–3725, <https://doi.org/10.1175/JCLI3455.1>.
- , —, B. E. Harden, and S. H. Mernild, 2015: The impact of resolution on the representation of southeast Greenland barrier winds and katabatic flows. *Geophys. Res. Lett.*, **42**, 3011–3018, <https://doi.org/10.1002/2015GL063550>.
- , D. H. Bromwich, A. B. Wilson, I. Renfrew, and L. Bai, 2016: Arctic System Reanalysis improvements in topographically forced winds near Greenland. *Quart. J. Roy. Meteor. Soc.*, **142**, 2033–2045, <https://doi.org/10.1002/qj.2798> <https://doi.org/10.1002/QJ.2798>.
- Nakamura, H., A. Nishina, and S. Minobe, 2012: Response of storm tracks to bimodal Kuroshio path states south of Japan. *J. Climate*, **25**, 7772–7779, <https://doi.org/10.1175/JCLI-D-12-00326.1>.
- Nakanishi, M., 2001: Improvement of the Mellor–Yamada turbulence closure model based on large-eddy simulation data. *Bound.-Layer Meteorol.*, **99**, 349–378, <https://doi.org/10.1023/A:1018915827400>.

- , and H. Niino, 2004: An improved Mellor–Yamada level-3 model with condensation physics: Its design and verification. *Bound.-Layer Meteor.*, **112**, 1–31, <https://doi.org/10.1023/B:BOUN.0000020164.04146.98>.
- , and —, 2006: An improved Mellor–Yamada level-3 model: Its numerical stability and application to a regional prediction of advection fog. *Bound.-Layer Meteor.*, **119**, 397–407, <https://doi.org/10.1007/s10546-005-9030-8> <https://doi.org/10.1007/S10546-005-9030-8>.
- Neu, U., and Coauthors, 2013: IMILAST: A community effort to intercompare extratropical cyclone detection and tracking algorithms. *Bull. Amer. Meteor. Soc.*, **94**, 529–547, <https://doi.org/10.1175/BAMS-D-11-00154.1>.
- Ogawa, F., H. Nakamura, K. Nishii, T. Miyasaka, and A. Kuwano-Yoshida, 2012: Dependence of the climatological axial latitudes of the tropospheric westerlies and storm tracks on the latitude of an extratropical oceanic front. *Geophys. Res. Lett.*, **39**, L05804, <https://doi.org/10.1029/2011GL049922>.
- Otte, T. L., C. G. Nolte, M. J. Otte, and J. H. Bowden, 2012: Does nudging squelch the extremes in regional climate modeling? *J. Climate*, **25**, 7046–7066, <https://doi.org/10.1175/JCLI-D-12-00048.1>.
- Papritz, L., S. Pfahl, H. Sodemann, and H. Wernli, 2015: A climatology of cold air outbreaks and their impact on air–sea heat fluxes in the high-latitude South Pacific. *J. Climate*, **28**, 342–364, <https://doi.org/10.1175/JCLI-D-14-00482.1>.
- Parfitt, R., A. Czaja, S. Minobe, and A. Kuwano-Yoshida, 2016: The atmospheric frontal response to SST perturbations in the Gulf Stream region. *Geophys. Res. Lett.*, **43**, 2299–2306, <https://doi.org/10.1002/2016GL067723>.
- , —, and Y.-O. Kwon, 2017: The impact of SST resolution change in the ERA-Interim reanalysis on wintertime Gulf Stream frontal air–sea interaction. *Geophys. Res. Lett.*, **44**, 3246–3254, <https://doi.org/10.1002/2017GL073028>.
- Powers, J. G., and Coauthors, 2017: The Weather Research and Forecasting Model: Overview, system efforts, and future directions. *Bull. Amer. Meteor. Soc.*, **98**, 1717–1737, <https://doi.org/10.1175/BAMS-D-15-00308.1>.
- Ralph, F. M., and Coauthors, 2017: Atmospheric rivers emerge as a global science and applications focus. *Bull. Amer. Meteor. Soc.*, **98**, 1969–1973, <https://doi.org/10.1175/BAMS-D-16-0262.1>.
- Rattan, S., P. G. Myers, A.-M. Treguier, S. Theetten, A. Biastoch, and C. Böning, 2010: Towards an understanding of Labrador Sea salinity drift in eddy-permitting simulations. *Ocean Modell.*, **35**, 77–88, <https://doi.org/10.1016/j.ocemod.2010.06.007> <https://doi.org/10.1016/J.OCEMOD.2010.06.007>.
- Ricchi, A., M. M. Miglietta, P. P. Falco, A. Benetazzo, D. Bonaldo, A. Bergamasco, M. Sclavo, and S. Carniel, 2016: On the use of a coupled ocean–atmosphere–wave model during an extreme cold air outbreak over the Adriatic Sea. *Atmos. Res.*, **172–173**, 48–65, <https://doi.org/10.1016/j.atmosres.2015.12.023> <https://doi.org/10.1016/J.ATMOSRES.2015.12.023>.
- Ricciardulli, L., and F. J. Wentz, 2015: A scatterometer geophysical model function for climate-quality winds: QuikSCAT Ku-2011. *J. Atmos. Oceanic Technol.*, **32**, 1829–1846, <https://doi.org/10.1175/JTECH-D-15-0008.1>.
- Roberts-Jones, J., E. K. Fiedler, and M. J. Martin, 2012: Daily, global, high-resolution SST and sea ice reanalysis for 1985–2007 using the OSTIA system. *J. Climate*, **25**, 6215–6232, <https://doi.org/10.1175/JCLI-D-11-00648.1>.
- Rudeva, I., and S. K. Gulev, 2007: Climatology of cyclone size characteristics and their changes during the cyclone life cycle. *Mon. Wea. Rev.*, **135**, 2568–2587, <https://doi.org/10.1175/MWR3420.1>.
- Rudnick, D. L., G. Gopalakrishnan, and B. D. Cornuelle, 2015: Cyclonic eddies in the Gulf of Mexico: Observations by underwater gliders and simulations by numerical model. *J. Phys. Oceanogr.*, **45**, 313–326, <https://doi.org/10.1175/JPO-D-14-0138.1>.
- Sarafanov, A., and Coauthors, 2012: Mean full-depth summer circulation and transports at the northern periphery of the Atlantic Ocean in the 2000s. *J. Geophys. Res.*, **117**, C01014, <https://doi.org/10.1029/2011JC007572>.
- Semedo, A., K. Sušelj, A. Rutgersson, and A. Sterl, 2011: A global view on the wind sea and swell climate and variability from ERA-40. *J. Climate*, **24**, 1461–1479, <https://doi.org/10.1175/2010JCLI3718.1>.
- Sérazin, G., T. Penduff, S. Grégorio, B. Barnier, J.-M. Molines, and L. Terray, 2015: Intrinsic variability of sea level from global ocean simulations: Spatiotemporal scales. *J. Climate*, **28**, 4279–4292, <https://doi.org/10.1175/JCLI-D-14-00554.1>.
- , —, B. Barnier, J.-M. Molines, B. K. Arbic, M. Müller, and L. Terray, 2018: Inverse cascades of kinetic energy as a source of intrinsic variability: A global OGCM study. *J. Phys. Oceanogr.*, **48**, 1385–1408, <https://doi.org/10.1175/JPO-D-17-0136.1>.
- Sharmila, S., and K. J. E. Walsh, 2018: Recent poleward shift of tropical cyclone formation linked to Hadley cell expansion. *Nat. Climate Change*, **8**, 730–736, <https://doi.org/10.1038/s41558-018-0227-5> <https://doi.org/10.1038/S41558-018-0227-5>.
- Shields, C. A., and Coauthors, 2018: Atmospheric River Tracking Method Intercomparison Project (ARTMIP): Project goals and experimental design. *Geosci. Model Dev.*, **11**, 2455–2474, <https://doi.org/10.5194/gmd-11-2455-2018>.
- Skamarock, W. C., and Coauthors, 2008: A description of the Advanced Research WRF version 3. NCAR Tech. Note NCAR/TN-475+STR, 113 pp., <http://doi.org/10.5065/D68S4MVH>.
- Skofronick-Jackson, G., and Coauthors, 2017: The Global Precipitation Measurement (GPM) mission for science and society. *Bull. Amer. Meteor. Soc.*, **98**, 1679–1695, <https://doi.org/10.1175/BAMS-D-15-00306.1>.
- Small, R. J., S. P. Xie, L. O’Neill, H. Seo, Q. Song, P. Cornillon, M. Spall, and S. Minobe, 2008: Air–sea interaction over ocean fronts and eddies. *Dyn. Atmos. Oceans*, **45**, 274–319, <https://doi.org/10.1016/j.dynatmoce.2008.01.001>.
- , R. A. Tomas, and F. O. Bryan, 2014: Storm track response to ocean fronts in a global high-resolution climate model. *Climate Dyn.*, **43**, 805–828, <https://doi.org/10.1007/s00382-013-1980-9> <https://doi.org/10.1007/S00382-013-1980-9>.
- , F. O. Bryan, S. P. Bishop, and R. A. Tomas, 2019: Air–sea turbulent heat fluxes in climate models and observational analyses: What drives their variability? *J. Climate*, **32**, 2397–2421, <https://doi.org/10.1175/JCLI-D-18-0576.1>.
- Smirnova, J., and P. Golubkin, 2017: Comparing polar lows in atmospheric reanalyses: Arctic system reanalysis versus ERA-interim. *Mon. Wea. Rev.*, **145**, 2375–2383, <https://doi.org/10.1175/MWR-D-16-0333.1>.
- Stoll, P. J., R. G. Graversen, G. Noer, and K. Hodges, 2018: An objective global climatology of polar lows based on reanalysis data. *Quart. J. Roy. Meteor. Soc.*, **144**, 2099–2117, <https://doi.org/10.1002/qj.3309> <https://doi.org/10.1002/QJ.3309>.
- Studholme, J., and S. Gulev, 2018: Concurrent changes to Hadley circulation and the meridional distribution of tropical cyclones. *J. Climate*, **31**, 4367–4389, <https://doi.org/10.1175/JCLI-D-17-0852.1>.

- Tang, J., S. Wang, X. Niu, P. Hui, P. Zong, and X. Wang, 2017: Impact of spectral nudging on regional climate simulation over CORDEX East Asia using WRF. *Climate Dyn.*, **48**, 2339–2357, <https://doi.org/10.1007/s00382-016-3208-2> <https://doi.org/10.1007/S00382-016-3208-2>.
- Tegen, I., P. Hollrig, M. Chin, I. Fung, D. Jacob, and J. Penner, 1997: Contribution of different aerosol species to the global aerosol extinction optical thickness: Estimates from model results. *J. Geophys. Res.*, **102**, 23 895–23 915, <https://doi.org/10.1029/97JD01864>.
- Tilinina, N., S. K. Gulev, I. Rudeva, and K. P. Koltermann, 2013: Comparing cyclone life cycle characteristics and their interannual variability in different reanalyses. *J. Climate*, **26**, 6419–6438, <https://doi.org/10.1175/JCLI-D-12-00777.1>.
- , —, and D. H. Bromwich, 2014: New view of Arctic cyclone activity from the Arctic system reanalysis. *Geophys. Res. Lett.*, **41**, 1766–1772, <https://doi.org/10.1002/2013GL058924>.
- , A. Gavrikov, and S. K. Gulev, 2018: Association of the North Atlantic surface turbulent heat fluxes with midlatitude cyclones. *Mon. Wea. Rev.*, **146**, 3691–3715, <https://doi.org/10.1175/MWR-D-17-0291.1>.
- Tolman, H., 2003: Treatment of unresolved islands and ice in wind wave models. *Ocean Modell.*, **5**, 219–231, [https://doi.org/10.1016/S1463-5003\(02\)00040-9](https://doi.org/10.1016/S1463-5003(02)00040-9).
- Tréguier, A. M., S. Theetten, E. P. Chassignet, T. Penduff, R. Smith, L. Talley, J. O. Beismann, and C. Böning, 2005: The North Atlantic subtropical gyre in four high-resolution models. *J. Phys. Oceanogr.*, **35**, 757–774, <https://doi.org/10.1175/JPO2720.1>.
- Tsujino, H., and Coauthors, 2018: JRA-55 based surface dataset for driving ocean–sea-ice models (JRA55-do). *Ocean Modell.*, **130**, 79–139, <https://doi.org/10.1016/j.ocemod.2018.07.002> <https://doi.org/10.1016/J.OCEMOD.2018.07.002>.
- Viale, M., and M. N. Nuñez, 2011: Climatology of winter orographic precipitation over the subtropical central Andes and associated synoptic and regional characteristics. *J. Hydrometeorol.*, **12**, 481–507, <https://doi.org/10.1175/2010JHM1284.1>.
- Vihma, T., and Coauthors, 2014: Advances in understanding and parameterization of small-scale physical processes in the marine Arctic climate system: A review. *Atmos. Chem. Phys.*, **14**, 9403–9450, <https://doi.org/10.5194/acp-14-9403-2014> <https://doi.org/10.5194/ACP-14-9403-2014>.
- Wagner, J. S., A. Gohm, A. Dörnbrack, and A. Schäfler, 2011: The mesoscale structure of a polar low: Airborne lidar measurements and simulations. *Quart. J. Roy. Meteor. Soc.*, **137**, 1516–1531, <https://doi.org/10.1002/qj.857> <https://doi.org/10.1002/QJ.857>.
- Waite, M. L., and C. Snyder, 2009: The mesoscale kinetic energy spectrum of a baroclinic life cycle. *J. Atmos. Sci.*, **66**, 883–901, <https://doi.org/10.1175/2008JAS2829.1>.
- Waliser, D., and B. Guan, 2017: Extreme winds and precipitation during landfall of atmospheric rivers. *Nat. Geosci.*, **10**, 179–183, <https://doi.org/10.1038/ngeo2894> <https://doi.org/10.1038/NNGEO2894>.
- Woollings, T., J. M. Gregory, J. G. Pinto, M. Reyers, and D. J. Brayshaw, 2012: Response of the North Atlantic storm track to climate change shaped by ocean–atmosphere coupling. *Nat. Geosci.*, **5**, 313–317, <https://doi.org/10.1038/ngeo1438> <https://doi.org/10.1038/NNGEO1438>.
- Wu, L., J. E. Martin, and G. W. Petty, 2011: Piecewise potential vorticity diagnosis of the development of a polar low over the Sea of Japan. *Tellus*, **63A**, 198–211, <https://doi.org/10.1111/j.1600-0870.2011.00511.x> <https://doi.org/10.1111/J.1600-0870.2011.00511.X>.
- Yu, L., and R. A. Weller, 2007: Objectively analyzed air–sea heat fluxes for the global ice-free oceans (1981–2005). *Bull. Amer. Meteor. Soc.*, **88**, 527–539, <https://doi.org/10.1175/BAMS-88-4-527>.
- Zahn, M., and H. von Storch, 2008: A long-term climatology of North Atlantic polar lows. *Geophys. Res. Lett.*, **35**, L22702, <https://doi.org/10.1029/2008GL035769>.
- Zappa, G., L. Shaffrey, and K. Hodges, 2014: Can polar lows be objectively identified and tracked in the ECMWF operational analysis and the ERA-Interim reanalysis? *Mon. Wea. Rev.*, **142**, 2596–2608, <https://doi.org/10.1175/MWR-D-14-00064.1>.
- Zeng, X., and A. Beljaars, 2005: A prognostic scheme of sea surface skin temperature for modeling and data assimilation. *Geophys. Res. Lett.*, **32**, L14605, <https://doi.org/10.1029/2005GL023030>.
- Zhu, Y., and R. E. Newell, 1998: A proposed algorithm for moisture fluxes from atmospheric rivers. *Mon. Wea. Rev.*, **126**, 725–735, [https://doi.org/10.1175/1520-0493\(1998\)126<0725:APAFMF>2.0.CO;2](https://doi.org/10.1175/1520-0493(1998)126<0725:APAFMF>2.0.CO;2).
- Zieger, S., A. V. Babanin, W. E. Rogers, and I. R. Young, 2015: Observation-based source terms in the third-generation wave model WAVEWATCH. *Ocean Modell.*, **96**, 2–25, <https://doi.org/10.1016/j.ocemod.2015.07.014> <https://doi.org/10.1016/J.OCEMOD.2015.07.014>.
- Zolina, O., and S. K. Gulev, 2002: Improving the accuracy of mapping cyclone numbers and frequencies. *Mon. Wea. Rev.*, **130**, 748–759, [https://doi.org/10.1175/1520-0493\(2002\)130<0748:ITAOMC>2.0.CO;2](https://doi.org/10.1175/1520-0493(2002)130<0748:ITAOMC>2.0.CO;2).
- , and —, 2003: Synoptic variability of ocean–atmosphere turbulent fluxes associated with atmospheric cyclones. *J. Climate*, **16**, 2717–2734, [https://doi.org/10.1175/1520-0442\(2003\)016<2717:SVOOTF>2.0.CO;2](https://doi.org/10.1175/1520-0442(2003)016<2717:SVOOTF>2.0.CO;2).
- Zuo, H., M. A. Balmaseda, S. Tietsche, K. Mogensen, and M. Mayer, 2019: The ECMWF operational ensemble reanalysis–analysis system for ocean and sea ice: A description of the system and assessment. *Ocean Sci.*, **2019**, 779–808, <https://doi.org/10.5194/OS-15-779-2019>.